BIOMINERALIZATION OF INORGANIC NANOSTRUCTURES USING PROTEIN SURFACES

A Thesis
Presented to
The Academic Faculty

by

Kathryn N Bergman

In Partial Fulfillment
of the Requirements for the Degree
Master of Science in Materials Science and Engineering

Georgia Institute of Technology
Spring, 2008

BIOMINERALIZATION OF INORGANIC NANOSTRUCTURES USING PROTEIN SURFACES

Approved by:

Dr. Vladimir V Tsukruk, Advisor
School of Material Science and Engineering
Georgia Institute of Technology

Dr. Valeria Milam
School of Material Science and Engineering
Georgia Institute of Technology

Dr. Kyriaki Kalaitzidou
School of Mechanical Engineering
Georgia Institute of Technology

Date Approved: March 26th, 2008

ACKNOWLEDGEMENTS

I would like to thank my advisor, Professor Vladimir Tsukruk for the opportunity to conduct this research. I would also like to thank my committee members, Dr. Valeria Milam and Dr. Kyriaki Kalaitzidou.

I would like to thank Dr. Rajesh Naik, Joe Slocik, and the biotech group at Wright-Patterson Air Force Base for help in starting this project.

My appreciation goes out to those at Georgia Tech including my fellow SEMA lab members and especially Maneesh Gupta, Eugenia Kharlampieva, and Maryna Ornatska who helped me with experimental setup, samples, and advice. I would also like to thank Ben Weintraub for technical discussion and Yolande Berta at the GT Center for Nanostructure Characterization for SEM and TEM assistance.

Finally, I would like to express my greatest appreciation to Cosette, Sheila, Mary and other family members and close friends for their encouragement and continued support.

Funding for this research was provided by AFRL and AFOSR.

TABLE OF CONTENTS

ACKNOWLEDGEMENTS iii

LIST OF TABLES & SCHEMES vi

LIST OF FIGURES vii

LIST OF SYMBOLS AND ABBREVIATIONS x

SUMMARY xii

CHAPTER

1 Background 1

Biosynthesis with Proteins 2

Silk 4

Properties, Structure and Microstructure 4

Biomineralization Applications to Date 9

Zinc Oxide 13

General Properties and Applications 13

Wet Chemical Synthesis in Solution and on Surfaces 14

2 Objectives and Approach 22

Materials Selection and Experimental Setup 24

Sample Preparation 25

Silk Solution 25

Silk and Polymer Films 26

Growth of Zinc Oxide Nanostructures Using Peptide 26

Gold Nanoparticle Growth Using Silk 31

Sample Characterization 33

3 Results and Discussion 34

Gold Nanoparticle Synthesis Using Silk Films 34

ZnO1 Peptide Structure and Properties 43

ZnO Rod Growth Using Peptide on Organic Films 47

Growth on a Silk Film 48

Controlling Size and Density of Rods on Silk 51

Growth of ZnO on a Polymer Film 57

Insitu Growth of ZnO Within Silk Films 59

Vertical ZnO Nanorod Arrays on Polystyrene 63

Polymer and Peptide Surfaces 63

Controlling Size and Density of Vertical Rods 68

4 Conclusions 73

REFERENCES 77

LIST OF TABLES & SCHEMES

Table 1. Structure and property differences in spider and silkworm proteins/silk fibers [19-22] 6

Table 2. Dominant reactions in the formation of ZnO from $Zn(NO_3)_2$ and HMT $C_6H_{12}N_4$ [71] 17

Table 3. Difference in rod size in the presence and absence of ZnO1 peptide. Samples were held at RT for 24hrs and 65^oC for 24hrs, $Zn(NO_3)_2$ and HMT were kept at a 1:1 ratio of 0.1M concentration. 51

Table 4. Surface coverage density at different concentrations of $Zn(NO_3)_2$ and HMT. Samples were held at RT for 24hrs and 90^oC for 4hrs, $Zn(NO_3)_2$ and HMT were kept at a 1:1 ratio. 55

Table 5. Difference in rod size in the presence and absence of ZnO1 peptide. Samples were held at RT for 24hrs and 90^oC for 4hrs, $Zn(NO_3)_2$ and HMT were kept at a 1:1 ratio of 0.01M concentration. 55

Table 6. Matrix to control density of vertical nanorods by changing solution component concentrations 69

Table 7. Summary of wet deposition parameters effect on ZnO growth using a film of ZnO1 76

Scheme 1. Sample film assembly and growth of zinc oxide rods [85] 29

Scheme 2. Growth of Au NPs using a silk film and mounting for TEM analysis 32

Scheme 3. Film assembly for gold nanoparticle growth using silk templates 32

Scheme 4. Film assembly with an embedded peptide layer 60

Scheme 5. Setup change in which a larger volume of precursors was used and the placement of the wafer was changed to eliminate large aggregates 69

LIST OF FIGURES

Figure 1. Patterning of silver nanoparticles biosynthesized using a silver-binding peptide [9] 3

Figure 2. Bimetallic gold/palladium nanostructures created using a hybrid selectively binding peptide [12] 4

Figure 3. Different structural models proposed for spider dragline silk [25, 30-32] 8

Figure 4. SEM of AgCl nanocrystals (white areas) formed on a silk fiber [49] 10

Figure 5. Gold colloid and silk fibroin core-shell bioconjugate [55] 12

Figure 6. Gold shell on a spider silk fiber [51] 12

Figure 7. SEM of ZnO nanostructures grew at different zinc nitrate and HMT concentrations at 85˚C. (a) 0.001M for 8hr (b, c) 0.001M for 24hr (d) 0.0001M for 8 hr (e) 0.0001M for 24 hr and (f) 0.1M for 8hr [68] 16

Figure 8. SEM of ZnO nanorod arrays by Vayssierres on a) a silicon wafer and b) a ZnO nanostructured thin film [64] 19

Figure 9. ZnO patterned microarray (left) and ZnO on a PET filaments (right) [78] 20

Figure 10. ZnO nanorod arrays formed on a polyimide surface with an underlying gold layer using e-beam lithography [71] 20

Figure 11. Flower-like morphology grown from ZnO particles in the presence of a selectively binding peptide [79] 21

Figure 12. Polymer chemical structures from left to right: PAH, PSS, PAA, PS 24

Figure 13. Small and large silicon wafer specimens 28

Figure 14. Small silicon wafer (arrow) mounted on a piece of glass for spin casting (top left), same small silicon wafer with peptide drop covering the entire surface (top right), and the same sample placed in the spin coater (bottom) 28

Figure 15. Sample placement in HMT/zinc nitrate for ZnO growth of large sample in 20ml glass vial (A), small sample in 1.5ml plastic vial , and small sample floating in 20ml glass vial before (C) and after (D) ZnO growth 29

Figure 16. Process of analyzing a sample's surface coverage by setting a threshold and removing noise 30

Figure 17. Silk layer number compared with total film thickness, resulting in a linear relationship..... 35

Figure 18. Gold nanoparticles formed after exposing $(PAH+PSS)_5$+$silk_5$ film on silicon substrate to 0.1M $HAuCl_4$ for 2 hours 37

Figure 19. $(PAH+PSS)_{20}$+silk on a silicon substrate exposed to 1.6mM $HAuCl_4$ for 22 hrs..... 39

Figure 20. $(PAH+PSS)_{20}$+silk film suspended on a TEM grid exposed to 1.6mM $HAuCl_4$ for 22 hrs 40

Figure 21. Film of $(PAH+PSS)_{10}$+silk+$(PAH+PSS)_{10}$ freely suspended and exposed to 1.6mM $HAuCl_4$ for 22 hrs. 42

Figure 22. ZnO1 Chemical Structure GLHVMHKVAPPRGGGC 45

Figure 23. Model of ZnO1 peptide with sequence H2N-GLHVMHKVAPPRGGGC-OH 46

Figure 24. Hydrophobicity plot for ZnO1 showing hydrophobic regions of the sequence on the left 47

Figure 25. Zinc oxide rods formed on silk films A) in the presence and B) in the absence of ZnO1 after exposure to $Zn(NO_3)_2$ + HMT 1:1 bath , both at 0.1M for 24hrs at room temperature followed by 24hrs at 65°C. 50

Figure 26. ZnO grown after 24hrs at RT and then 2hrs at 65°C on silk plus ZnO1 (left) and on silk (right) in 0.1M of zinc nitrate/HMT 1:1 52

Figure 27. ZnO after 24hrs RT and 90° 4hrs in 0.1M zinc nitrate / HMT 1:1 solution on silk (B) and on silk with peptide drop cast (A) 53

Figure 28. ZnO after 24hrs RT and 4hrs 90° in 0.01M zinc nitrate / HMT 1:1 solution A) on silk with drop cast peptide and B) on silk 54

Figure 29. ZnO growth on polyelectrolyte surface PSS (left) and PAH (right) 57

Figure 30. ZnO grown on PAA (left) and PAA with peptide (right) 58

Figure 31. ZnO on polystyrene (top) and ZnO on polystyrene plus ZnO1 (bottom); the boundary where the peptide drop was cast and dried is clearly visible (bottom) 59

Figure 32. SEM of ZnO grown on (left) $silk_9$+ZnO1 and (right) $silk_9$+ZnO1+$silk_9$ films 60

Figure 33. Embedded ZnO grown at a peptide layer between two drop cast silk layers. 61

Figure 34. AFM height (left, scale 800nm) and phase (right) images of ZnO grown in a $silk_9$+ZnO1+$silk_9$ film; top is 5μm x 5μm, bottom 2μm x 2μm. Z-scale is 800nm (top) and 550nm (bottom)..... 62

Figure 35. AFM height image of silk film with a roughness of 4.8nm 64

Figure 36. AFM image of polystyrene surface spin cast from 0.2wt% solution (1x1μm scan, z-scale 5nm)..... 65

Figure 37. AFM image of ZnO1 spin cast on PS from a A) 20x20 B) 5x5 and C) 1x1μm scan 66

Figure 38. Vertical ZnO rods on PS and an unrinsed peptide layer. Grown in 0.1M zinc nitrate and HMT at RT 24hrs and then 65oC for 24hrs. 67

Figure 39. Vertical rods of Figure 38 but showing a different area of large precipitated aggregates which were common on the surface 68

Figure 40. ZnO grown on PS+ZnO1 in (left) 0.1M HMT and (right) 0.4M HMT, combined 1:1 with 0.1M zinc nitrate 71

Figure 41. ZnO grown on PS+ZnO1 in 0.1M HMT plus zinc nitrate A) 0.1M B) 0.125M and C) 0.15M 71

Figure 42. Graph comparing zinc nitrate concentration to percent surface covered by ZnO 72

Figure 43. Graph comparing zinc nitrate concentration to aspect ratio..... 72

LIST OF SYMBOLS AND ABBREVIATIONS

AFM	Atomic Force Microscopy
CVD	Chemical Vapor Deposition
HMT	Hexamethylenetetramine
hr	hour
pI	isoelectric point
LbL	Layer by Layer
M	Molar (concentration)
M	Molar (concentration)
nm	nanometer
^{o}C	degrees Celsius
PAA	Poly(acrylic acid)
PAH	Poly(allylamine hydrochloride)
PS	Polystyrene
PSS	Poly(sodium styrene sulfonate)
RMS	Roughness Mean Squared
rpm	rotations per minute
RT	Room Temperature
SEM	Scanning Electron Microscopy
TEM	Transmission Electron Microscopy
WCD	Wet Chemical Deposition
ZnO1	Peptide that selectively binds to zinc oxide and used in this study

Ala, A	Alanine
Arg, R	Arginine
Asn, N	Asparagine
Asp, D	Aspartic acid
Cys, C	Cysteine
Glu, E	Glutamic acid
Gln, Q	Glutamine
Gly, G	Clycine
His, H	Histidine
Ile, I	Isoleucine
Leu, L	Leucine
Lys, K	Lysine
Met, M	Mehionine
Phe, F	Phenylalanine
Pro, P	Proline
Ser, S	Serine
Thr, T	Threonine
Trp, W	Tryptophan
Tyr, Y	Tyrosine
Val, V	Valine

SUMMARY

In the work presented in this thesis, two biomaterials were investigated as thin films for the biomineralization of zinc oxide and gold NPs: a zinc oxide selectively binding peptide "ZnO1" and silk fibroin protein from the Bombyx Mori silkworm. Zinc oxide nanorods and gold nanoparticles both have interesting properties that can be used for a multitude of applications at the nanoscale. Biomineralization methods investigated here aims to synthesize these materials at ambient or near ambient conditions.

First, silk films were used to attempt reduction of gold nanoparticles. Silk has outstanding mechanical properties, including a unique combination of strength and toughness. We successfully synthesized gold nanoparticles at room temperature using a silk film. The silk film was able to reduce when on the surface or embedded between polyelectrolyte bilayers.

Second, biomineralization of zinc oxide nanorods was attempted using films of silk, silk + peptide, silk + peptide + silk, and polymer + peptide. Here we used films to explore the effect of peptide film presence and the effect of changing wet chemical deposition parameters. Lastly, we attempted to optimize surface and growth parameters such as time, temperature, and solution concentration to achieve vertical zinc oxide nanorods on an entirely organic surface.

For surface growth, silk and polystyrene proved successful underlying layers for the formation of a ZnO1 film due to hydrophobic interactions between the peptide and

the organic film. By minimizing the roughness of the peptide layer, zinc oxide nanorod arrays were grown vertically via wet chemical deposition from an entirely organic template of polystyrene + peptide. Control of size and density of the rods across the surface was achieved by using a ZnO1 peptide surface and changing the time, temperature, and precursor solution concentrations. In addition, by embedding the peptide layer between two silk layers, we could successfully grow encapsulated rods in between two silk films.

CHAPTER 1

BACKGROUND

Control of materials at the nanoscale level is vital to the creation of new, novel nano-composites and nano-devices. Although there has been much progress with the synthesis of nanostructures, severe limitations exist with current technologies. The harsh temperatures used for a majority of inorganic synthesis severely limit the compatible surfaces and composites. For example, the synthesis of vertical zinc oxide nanorod arrays for use in sensors and electronics cannot be done easily on organic or biocompatible substrates. The harsh conditions of CVD are not compatible with low melting temperature materials [1]. Wet chemical deposition can be done at low temperatures but can not to date produce usable morphologies such as vertical nanorods on surfaces without using an underlying inorganic layer (i.e., zinc oxide or gold) [2].

Biomineralization is defined as the study of the formation, structure and properties of inorganic solids deposited in biological systems [3]. Biomineralization methods can create incredibly precise and intricate structures, commonly under ambient conditions [4]. Harnessing proteins' ability to create inorganic structures under mild conditions could open up new morphology, substrate, and application possibilities not otherwise achievable.

Biosynthesis with Proteins

Nature can control the formation of inorganic materials by specific proteins. Specific proteins in numerous organisms form intricate nanostructures under mild conditions. This ability has attracted the attention of nanotechnology scientists who aim to use proteins towards a similar goal: to control the formation of intricate inorganic nanostructures at near ambient conditions for incorporation into endless applications. For example, the ability to form nanoscale features with molecular level control would enable the "bottom up" approach in manufacturing chips. Several inorganics have been synthesized or patterned with biomaterials, for example tobacco mosaic virus liquid crystals to form silica nanoparticles [5], tyrosine to form gold core – silver shell nanoparticles [6], ferritin to bind titania and create a 3D patterned multilayered structures [7], and silk which will be described in more detail later.

In addition to these naturally occurring proteins with biomineralization capabilities, peptides with an affinity for inorganic matter can be designed. Using a combinatorial library approach called *phage display* for selection, peptides sequences can be identified for a specific metal or oxide. Phage display uses a library of peptides with random sequences and exposes them to the inorganic material [8]. After sequential washes to remove weak or non-bound sequences, the remaining sequences are multiplied using bacteria. This process of washing and amplifying is repeated to achieve a single peptide with the highest affinity to the target material.

Several inorganic materials have had peptides identified using methods including phage display. A list of twelve materials with amino acid sequences listed for each

peptide identified was recently summarized in a review by Sarikaya et al. [4]. These peptides can then be used to create micro- or nano-structures of that inorganic material, control particle distribution and size. For example, silver nanoparticles were recently synthesized and patterned using a selective peptide in Figure 1 [9]. Other materials synthesized to date include rutile (TiO_2) [10] and $CaCO_3$ [11].

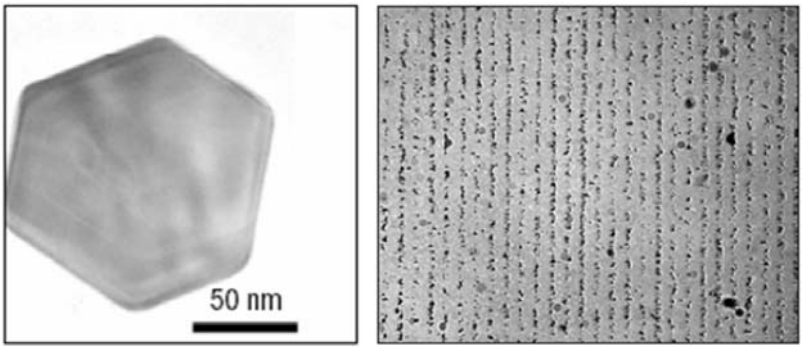

Figure 1. Patterning of silver nanoparticles biosynthesized using a silver-binding peptide [9]

In addition, these peptides can be combined to synthesize bimetallic nanostructures. In a recent paper by Slocik et al, gold nanoparticles were formed with a multifunctional peptide and then smaller palladium nanoparticles were formed around each peptide-coated gold nanoparticle in solution [12]. In addition, the peptide could also be used for its affinity to a palladium surface, resulting in a Pd surface dabbled with gold.

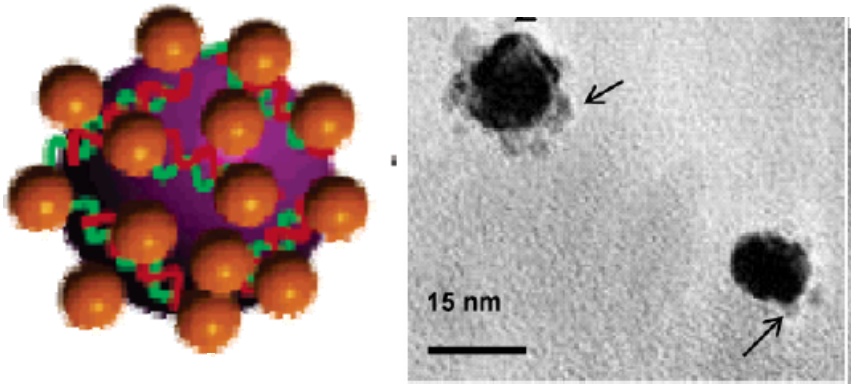

Figure 2. Bimetallic gold/palladium nanostructures created using a hybrid selectively binding peptide [12]

Using peptides specific for inorganic binding and nucleation that can be combinded, endless possibilities begin to emerge. For example, the assembly of hybrid materials at the molecular level could make bottom-up self assembly techniques for electronic applications.possible.

Silk

Properties, Structure, and Microstructure

Silk is a versatile biomaterial with outstanding mechanical properties. Silkworm silk, known as the silk protein *fibroin*, has been used for sutures in biomedical applications for many years [13]. The fiber spun by the silkworm *Bombyx Mori* is actually two filaments simultaneously and continuously extruded through a spinneret from a pair of silk glands within the worm. These are cemented together during the spinning process. Relatively large amounts of silk are harvestable from silkworms compared to spider silk, giving it a practical advantage for applications.

Silk is known and used for its tensile strength, elasticity, toughness, and biocompatibility. As a complex biological material, the structure of silk seen in Table 1 highly affects mechanical and physical properties. Property variations related to structure differences are based on factors ranging from the basic chemical makeup of repeating motifs to the materials' level of crystallinity. The general amino acid sequences in beta sheets are thought to be responsible for the impressive mechanical properties of B. mori silkworm silk. The table also summarizes the general molecular structure and amino acid sequences present in the protein and mechanical property values.

Properties of silk listed in Table 1 are not to be taken as absolutes but instead as general experimental values. Differences between species, spinning conditions (i.e., spider body temperature) [14], and spinning speeds [15] can create values which vary from publication to publication [14, 16-18].

Table 1. Structure and property differences in spider and silkworm proteins/silk fibers [19-22]

Character	*Bombyx mori fibroin*	*Spidroin*
Repeating motifs	GAGAGS	GPGGX
	GAGAGY	GPGQQ
		$(A)_n$
		$(GA)_n$
		GGX
Crystalline regions	Poly-Gly-Ala blocks	Poly-Ala blocks
β-sheet crystals content %	40-50%	35% (Araenus MA)
# of silk types	One	Up to eight

Mechanical properties	*Mulberry silk (B. mori)*	*Spider silk (MA)*
Modulus (GPa)	15-17	11-13
Strength σ_{max} (GPa)	0.6	0.9-1.0
Toughness (MJ m^{-3})	70	160
Extension (%)	18	27
Behavior in water	Little change in silk shape/length	Supercontraction of dragline
Mass production	B. mori (domesticated) grown for millennia	Only small quantities achieved

Major structural details in the fibroin protein contribute to properties. Gly-X (G-X) repeats cover 94% of the sequence. Residue X in the Gly-X is, with rounding, Ala (A) 64% of the time, Ser (S) 22% and Tyr (Y) 10% [23] . The hexapeptides GAGAGS and GAGAGY of silk fibroin make up roughly 70% of the general Poly-Gly-Ala blocks that make up crystalline regions. These two repeating motifs promote a secondary

structure of anti-parallel β-pleated sheets, formed by the folding of the protein's crystalline region [20].

Silk possesses a unique combination of strength and toughness, unlike many other structural polymers. It is generally understood that the highly stable secondary structure contributes to the impressive mechanical properties. The strength of silk is attributed in part to β-sheets in the crystalline regions and also, the hydrophobic interactions between those regions [24]. Glycine's presence in silkworm crystalline blocks (absent in spider silk) allows conformational variability. Silkworm silk is stiff but brittle compared to spider silk, due to the higher level of crystallinity [19].

Beyond the molecular scale, there are several thoughts on the detailed composition and degree of crystallinity in silk on a micro-scale [25-27]. Silks have alternating hydrophobic (crystalline) and less hydrophobic (non-crystalline) blocks [28]. Models have been suggested to explain the makeup of silk β structures and how they might assemble to form sheets in silk [29]. In the earliest models, nanocrystallites are shown surrounded with amorphous regions to form β structures (Figure 3A) [30]. Two types of crystalline regions were found after further H NMR studies, which contradict the previous model. These two crystalline regions can be described as highly oriented and tightly packed and the other as poorly oriented and less dense as in Figure 3B, red and green arrows respectively [31]. Recently, a third model using 2D solid state NMR results proposed helical structures in the glycine-rich amorphous region (Figure 3C) [32]. The β sheets are alanine (red lines) with glycine predominantly as 3_1-helical parts (blue curls).

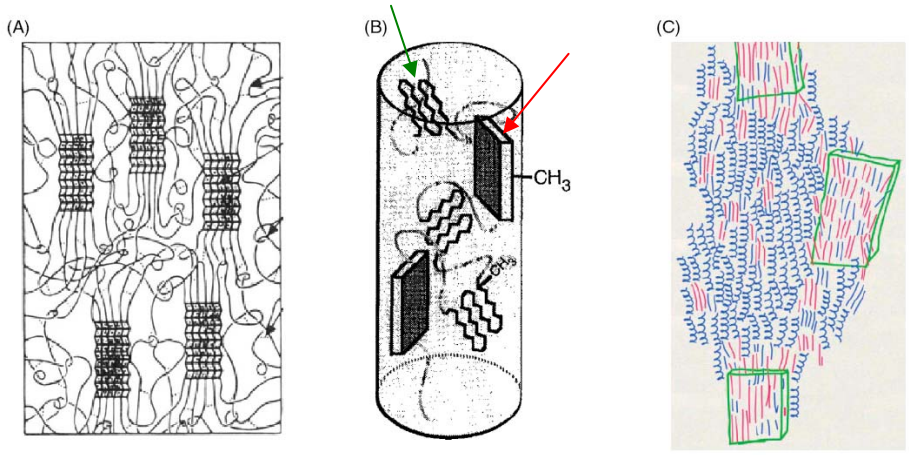

Figure 3. Different structural models proposed for spider dragline silk [25, 30-32]

Silkworm silk fibroin can be dissolved and regenerated from ionic liquids and water [33]. From there, new materials can be regenerated with the ability to control level of crystallinity and mechanical properties [34]. In aqueous solution, hydrogels and films have formed which, much like raw fibers, have good mechanical properties [35]. Extremely robust ultrathin films can be formed with spin assisted Layer-by-Layer (LbL) techniques, achieving thicknesses <100nm. Mechanical properties of these LbL ultrathin films were tested in compression and tension modes and found to be outstanding with an elastic modulus of 6.5 GPa and an ultimate strength approaching 100 MPa [35]. Electrospinning has been done using reconstituted silks from biologically spun fibers [36] as well as silk in aqueous solution with PEO addition [37].

In regenerated silk, three states can exist: random coil (low concentrations of fibroin), Silk I (α), and Silk II (β). Silk I is a meta-stable form not well defined; it is described in literature as both lacking second order structure and having well formed

crystals [38, 39]. Most information, on the other hand, points to semi-ordered Silk I states being transitional before forming Silk II.

Various chemical and physical methods can induce a transition. Exposure to methanol, physical shear, stretching, annealing with water, and heat does not just induce random conformation transformation; these can aid in the control of crystallinity, hydrophobicity, mechanical properties, and degradation of the newly formed materials [34, 35]. Polar solvents such as water and methanol however tend to reduce the modulus and strength of the fiber [40].

Biomineralization Applications to Date

The majority of applications exploit silk's biocompatibility for biomedical purposes. In addition to being reliable under many temperatures and humidity levels, silk exhibits good mechanical strength when wet, resists enzymatic cleavage, and has high oxygen and drug permeability [41]. Silk sutures patented in 1969 are one of the oldest uses of silk [13]. As a wound dressing, silk can retain water and keep an area moist. It is also transparent so the wound is visible as it heals [42]. Silk has been shown to increase cell adhesion and growth when used to coat scaffolds for human fibroblasts [43], coat films for rat cells, and as electrospun fibers [44]. Modifications with 1,2 cyclohexanedione increases fibroblast cell adhesion [45] as does RGD (Arginine-Glycine-Aspartic acid) modified fibroin matrices with human bone marrow stromal cells [46]. Other uses include possible substitution for collagen in cultivating mammalian cells and a net for human cells where a tissue like structure will form around a silk net [47].

Studies have shown that external pH can regulate permeability of a silk membrane which then lends itself to drug delivery applications [48].

Biomineralization applications include the use of silk as a template for the growth of inorganic structures. Silk can serve as a substrate for inorganic growth or a matrix whose chemical structure promotes the formation of metal nanoparticles within. Work thus far on creating inorganics with the use of silk has been done with fibers [49-54]. Biomimic composites for bone using silk-apatite have been well researched [50]. The tyrosine groups in natural silk are thought to aid in the reduction of metal nanoparticles such as silver, palladium, and gold [6]. Silver chloride nanocrystals were formed on a silk fiber by the sequential dipping in silver nitrate and sodium chloride with a water rinse step between each dip, shown below in Figure 4 [49].

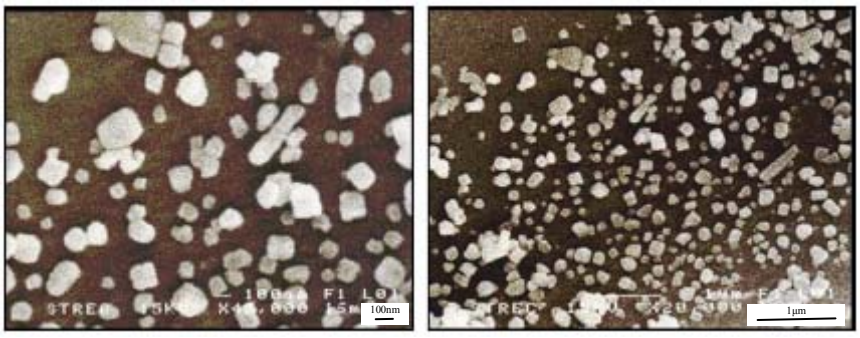

Figure 4. SEM of AgCl nanocrystals (white areas) formed on a silk fiber [49]

Palladium has been biomineralized by simply soaking a silk fiber in $Pd(OAc)_2$ and then in a MeOH reducing agent. It was shown that the dipping of silk fiber in PDADMAC and silver nanoparticles capped with PMA formed a film with antimicrobial properties [53]. Monodisperse gold nanoparticles were reduced in situ by the silk fibroin protein to form a core-shell gold colloid-silk fibroin bioconjugate at room temperature shown below in Figure 5 [55]. Although not on silk fibroin, it is worth noting gold has also been reduced to form a shell around spider silk fibers seen below in Figure 6.

The ability to reduce gold nanoparticles is important as gold nanoparticle composites are becoming widely used in several fields. Organic-gold nanoparticle composites have been used for a range of biomedical and sensing applications, a few of which include anti-bacterial coatings, surface enhanced Raman scattering (SERS), extremely sensitive thin film sensors [56] and for use in plastic "memory" devices [57]. These require monodispersity and optimization of gold nanoparticle size for the select application.

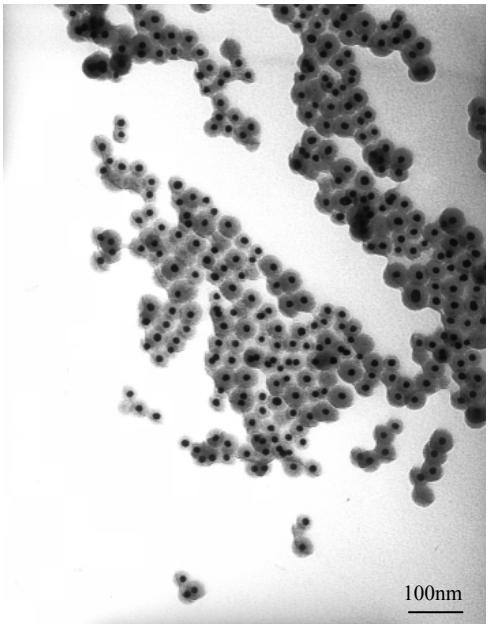

Figure 5. Gold colloid and silk fibroin core-shell bioconjugate [55]

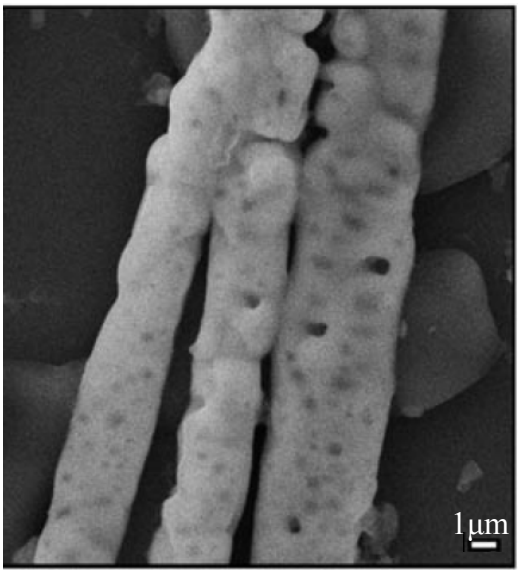

Figure 6. Gold shell on a spider silk fiber [51]

Inorganic/bio composite work involving silk also includes the growth of cadmium sulfide which was crystallized using silk as a membrane [58] and the growth of nano-TiO_2 [59] which was grown based on the sol-gel technique. Silk was mixed with titanium n-butoxide, and then cast to form titania nanoparticles.

Issues that are detrimental to applications exist but are generally not severe, such as degradation of silk. Degradation can be viewed as advantageous in some cases. Clean silk fibers are largely inert as evidence shows but the presence of sericin (removed during cleaning) can trigger an immune response if not completely separated [60]. The intrinsic variability of silk in harvested threads can be addressed with advanced processing to achieve more precise and predictable properties [19].

With the versatility of silk, the biocompatibility, and the more recent advances in template and composite interactions, silk could become an important nanocomposite material.

Zinc Oxide

General Properties and Applications

Zinc oxide is an interesting material because of both its intrinsic properties and the crystal structures synthesizable to date. ZnO is a direct band gap semiconductor (3.37 eV) with large excitation binding energy (60meV), has near UV emission and transparent conductivity, exhibits piezoelectric property resulting from its non-centrosymmetric structure, is bio-safe and bio-compatible [61]. Potential applications such as MEMS, sensors, transducers, solar cells, UV lasers, nanogenerators, and biomedical applications

without coatings are possible because of these fundamental characteristic properties of ZnO.

Zinc oxide is synthesized by means of chemical vapor deposition (CVD), electrodeposition, and wet chemical deposition. Restrictions on device and processing conditions are unnecessarily imposed as CVD is done at relatively extreme conditions [62]. Many groups have investigated and reported structures such as nanowires, nanorods, nanotubes, nanobelts, nanocombs, nanosprings, nanorings, nanobows, and nanopropellers grown from solution [61]. Wet chemical deposition is often preferred because it is highly reproducible, does not require expensive setup, useful functional groups can be incorporated during nanostructure growth making them easily dispersible in common solvents, and standard purification techniques are available such as filtration and centrifugation [63-65]. In addition, wet chemical deposition is compatible with the mild, low or room temperature processing necessary for crystal formation on organic materials.

Wet Chemical Synthesis in Solution and on Surfaces

Wet chemical deposition (WCD) of zinc oxide is advantageous because of the low temperatures used, as low as 60˚C; extremely small widths of nanorods possible, less than 10nm; and the high aspect ratios achieved, greater than 200. The mild conditions of WCD are compatible with soft materials including polymers and biological materials.

The hydrolysis and condensation reactions of zinc salts under many different conditions result in one dimensional ZnO crystals [66]. At pH < 9, an additive such as

HMT or dimethylamineborane (DMBA) is used to promote one-dimensional (nanorod) precipitation. Lowering pH can slow down the reaction and results in well defined faces on structures and higher quality films [67].

A solution of zinc nitrate $ZnO(NO_3)_2$ and hexamethyltetramine HMT $(CH_2)_6N_4$ is used often to form ZnO structures due to its simplicity. The two are both soluble in water and when mixed together, form zinc oxide crystals at a low temperature. For a one-to-one mole ratio, typically 0.1 M, one-dimensional structures with a few hundred nanometer diameter and 1-3 μm lengths can be obtained [68]. The nanorods' diameter is typically proportional to the $Zn(NO_3)_2$ and HMT concentration. Although lower concentrations down to 0.0001M reduce the diameter and increase aspect ratios of nanorods, bundling can occur and the distribution of lengths are more broad [64, 68, 69]. Figure 7 shows result by Ho et al [68] of various sizes of nanorods grown under different precursor and time conditions. In another study, zinc nitrate salt was found to be the limiting reagent for one-dimensional growth. It was shown that a greater molar concentration of zinc nitrate to HMT yields higher aspect ratio nanorods, at the expense of increased width. The opposite is observed when a greater molar concentration of HMT is used [70].

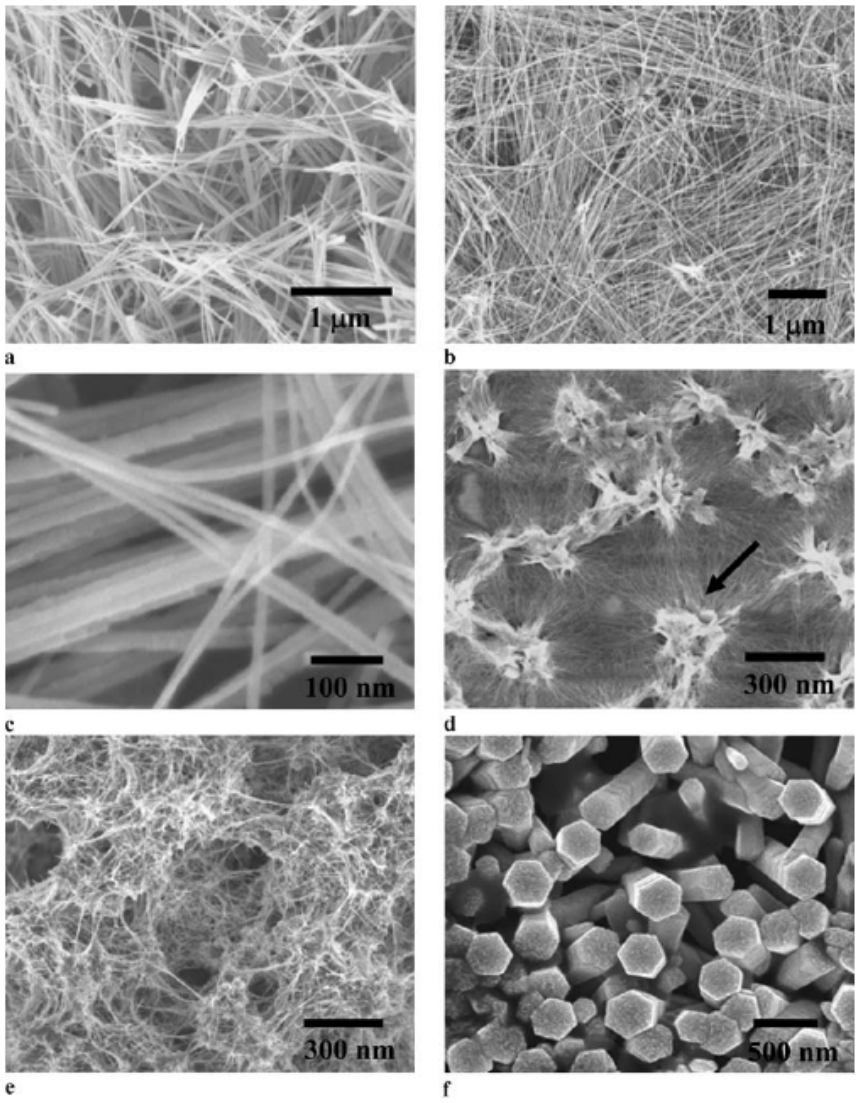

Figure 7. SEM of ZnO nanostructures grew at different zinc nitrate and HMT concentrations at 85°C. (a) 0.001M for 8hr (b, c) 0.001M for 24hr (d) 0.0001M for 8 hr (e) 0.0001M for 24 hr and (f) 0.1M for 8hr [68]

Zinc nitrate and HMT are commonly used to create zinc oxide nanostructures, although the exact role of HMT in reaction is still under debate. The dominant chemical reactions summarized recently by Weintraub et al. are shown below in Table 2 [71].

Table 2. Dominant reactions in the formation of ZnO from $Zn(NO_3)_2$ and HMT $C_6H_{12}N_4$ [71]

$C_6H_{12}N_4 + 6H_2O \leftrightarrow 6CH_2O + 4NH_3$	(1)
$C_6H_{12}N_4 + Zn^{2+} \rightarrow [Zn(C_6H_{12}N_4)]^{2+}$	(2)
$NH_3 + H_2O \leftrightarrow NH_4^+ + OH^-$	(3)
$Zn^{2+} + 4NH_3 \rightarrow Zn(NH_3)_4^{2+}$	(4)
$Zn^{2+} + 4OH^- \rightarrow Zn(OH)_4^{2-}$	(5)
$Zn(NH_3)_4^{2+} + 2OH^- \rightarrow ZnO + 4NH_3 + H_2O$	(6)
$Zn(OH)_4^{2-} \rightarrow ZnO + H_2O + 2OH^-$	(7)

It has been suggested that hydroxide ions are formed by the decomposition of HMT and the hydrothermal reduction of Zn^{2+} precursor to form ZnO [72]. Prior to heating, the solution mixture should be aged to allow the formation of the Zn-amine complex. Heating decomposes the Zn-amine complex, releasing Zn^{2+} ions which under hydrothermal conditions, subsequently form $Zn(OH)_2$ and ZnO nanoparticles as in equation (6) and (7) of Table 2. Given substantial time, 3-5 nm ZnO crystallites in the form of white precipitates can be seen before heating, which later act as nucleation sites for one-dimensional growth. A minimum temperature of 60°C and up to 200°C has been

reported for the hydrothermal reaction, such that shorter reaction time is needed at higher temperature to form one-dimensional structures [73, 74].

On various crystalline and amorphous substrates, wet chemical deposition of zinc oxide is done with low temperatures under mild conditions. Growth independent of the substrate is only achieved however with the use of an inorganic layer, typically zinc oxide seeds which brings with it unique processing problems. To improve adhesion of the seed particles to the substrate, samples typically need to be annealed at temperatures of 150°C or higher; verticality of rods grown from random directional seeds is another problem though annealing at a temperature of 350°C can improve vertical alignment of rods [75-77]. These high temperatures however spoil the advantage of wet chemical deposition over other methods such as CVD. Biomineralization using a selectively binding peptide for zinc oxide instead of inorganic seeds becomes an attractive solution for the controlled synthesis of zinc oxide at low temperatures.

The enhanced verticality from the use of a crystalline substrate or seed layer can be seen in Figure 8, the nanorods have been grown on both a silicon substrate and a ZnO nanostructured thin film. The dense growth near the surface is random in direction and as neighbor nanorods in close proximity grow at the same rate, they eventually restrict each other's horizontal growth. The result is fairly well aligned but not completely perpendicular nanorods. This is only achieve with a completely dense forest of rods; vertical rods not in contact with each other can not be synthesized in this way.

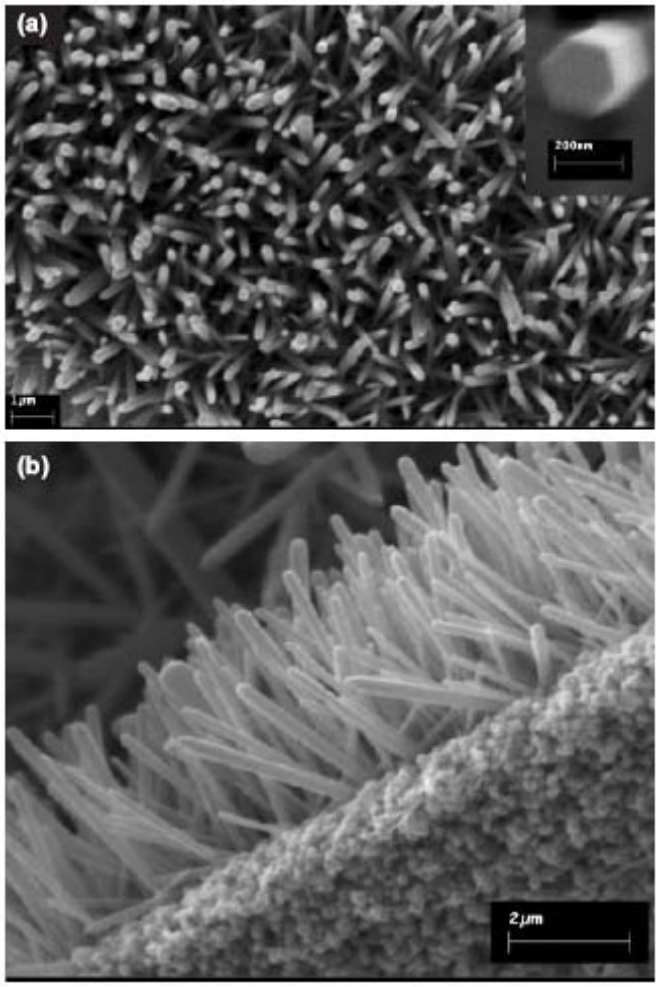

Figure 8. SEM of ZnO nanorod arrays by Vayssierres on a) a silicon wafer and b) a ZnO nanostructured thin film [64]

On polymer surfaces, there are few examples of successful formation and patterning of zinc oxide nanorods. A recent study by Morin et al. [78] synthesized randomly oriented microarrays on polycarbonate surfaces and flexible PET filaments (Figure 9). Creating regions with different surface energies by selectively functionalizing the surface either suppressed or promoted heterogeneous nucleation [78].

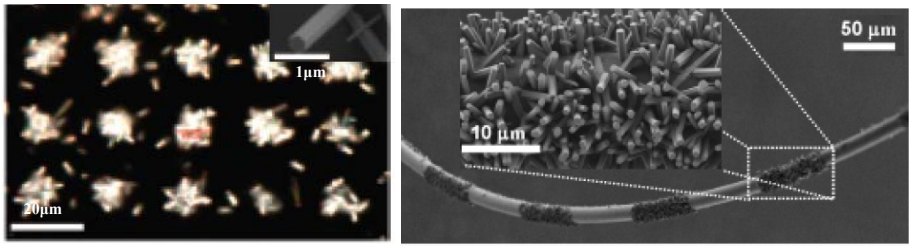

Figure 9. ZnO patterned microarray (left) and ZnO on a PET filaments (right) [78]

Other patterning and improved verticality has been achieved by incorporating an inorganic layer under the polymer. Weintraub et al. patterned ZnO by using e-beam lithography and a PMMA mask to determine positions of growth on a polyimide surface. To enhance nucleation, an intermediate gold layer with an applied potential was used [71]. There are no studies to date demonstrating controlled growth of vertical zinc oxide nanorods on completely organic templates.

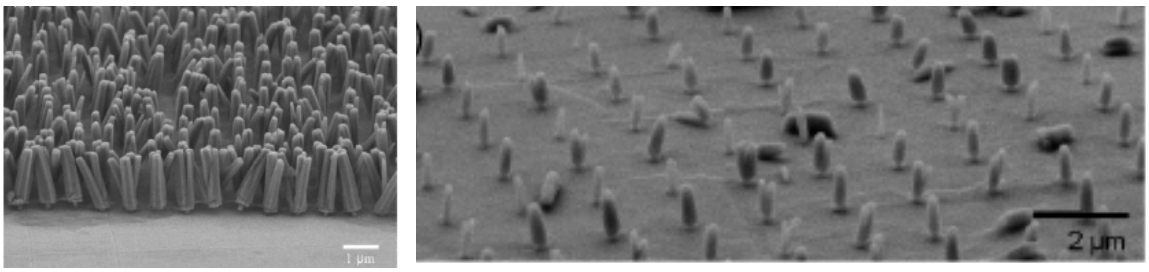

Figure 10. ZnO nanorod arrays formed on a polyimide surface with an underlying gold layer using e-beam lithography [71]

Although novel ZnO structures have been synthesized using biomineralization approaches, morphologies are typically impractical and have not been investigated towards the use in an application. Other groups have investigated zinc oxide selectively binding peptides towards the control of crystal morphology. In a study by Umetsu et al [79], a zinc oxide flower-type morphology was achieved with a peptide as seen below in Figure 11. The peptide was modified from the original 12 amino acid sequence with GGGSC, a glycine linker and a cysteine at the C-terminus which immobilized the peptide on the surface and proved to be critical for the synthesis of ZnO from $Zn(OH)_2$ [79]. There are no studies to date using a selectively binding peptide or other biomineralization method to control the growth or patterning of zinc oxide nanorod structures on a surface.

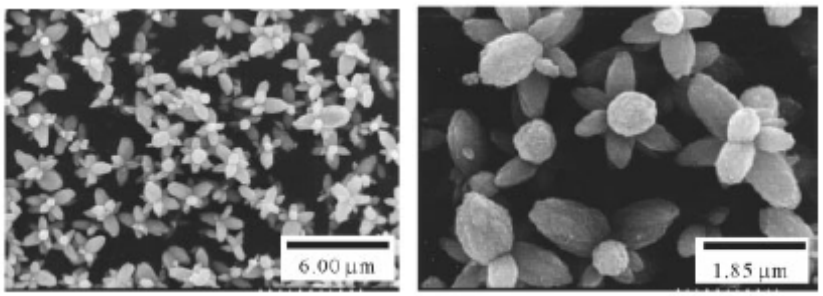

Figure 11. Flower-like morphology grown from ZnO particles in the presence of a selectively binding peptide [79]

CHAPTER 2

OBJECTIVES AND APPROACH

The research presented in this thesis is conducted to synthesize organic/inorganic nanocomposites using biomaterial films and ambient conditions of wet chemical synthesis. Ambient or low temperature conditions are necessary for soft material and biomatieral compatibility. Biomineralization using a zinc oxide selectively binding peptide and silk fibroin can potentially control the formation of nanostructures under conditions not achievable with other synthesis methods for novel applications.

Ultimate Goals:

- Investigate and control the formation of gold nanoparticles dispersed on/within a thin silk film
- Achieve an array of vertical zinc oxide nanorods grown from a completely organic system

More specifically, this will involve the following steps:

- Create gold nanoparticles using a silk film. This will be done by soaking in $HAuCl_4$ a film assembly of an underlying sacrificial layer upon which twenty polyelectrolyte bilayers and a silk film will be cast. Different preparation and soaking conditions will be changed to investigate the

effect on size, shape, and density of nanoparticles. The sample will be released from the substrate and placed on a nylon grid for TEM analysis.

- Investigate if/how ZnO1 peptide controls the growth of zinc oxide nanorods on various organic surfaces. This will be done by spin casting polymer and silk films onto a silicon wafer, drop casting a peptide film, then exposing the sample to a zinc nitrate and HMT bath for oxide growth.
- Change oxide growth parameters to see the effect on the growth of zinc oxide rods. This will be done by changing the growth time, temperature, and zinc nitrate/HMT concentration.
- Create a smooth layer of peptide and conditions favorable for the growth of vertical nanorods. This will be done by changing the method of how the peptide film is deposited and possibly using a rinse step.
- Optimize conditions for a uniform array of vertical nanorods with control over dimensions and density on an organic surface. This will be done by changing zinc nitrate and HMT concentrations.

Materials Selection and Experimental Setup

A selectively binding peptide for zinc oxide, "ZnO1" and silk fibers were provided in collaboration with the Biotechnology group in the Materials and Manufacturing Directorate at Wright-Patterson Air Force Base in Dayton, Ohio. The peptide was identified using phage display technique and custom ordered from New England Peptide Co. Silk cocoons were harvested and cleaned at Wright-Patterson. They were received as fibers and further processed at Georgia Tech.

Polymers used as substrates for zinc oxide growth included poly allylamine hydrochloride (PAH) M_w=70,000, poly(sodium styrene sulfonate) (PSS) M_w=70,000, poly(acrylic acid) (PAA) M_w unknown and polystyrene (PS) M_w=250,000 seen in Figure 12.

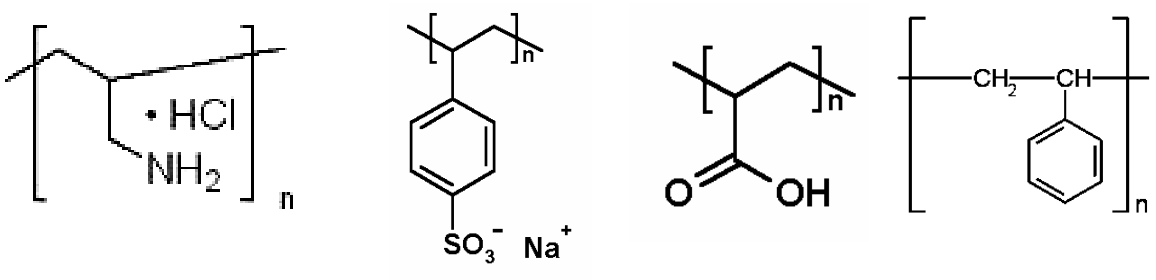

Figure 12. Polymer chemical structures from left to right: PAH, PSS, PAA, PS

Silk and polymer films were created on atomically flat polished silicon wafers of the [100] orientation (Semiconductor Processing, Co.).

The zinc oxide crystals were grown in a solution made with $Zn(NO_{3)2}6H_2O$ (zinc nitrate hexahydrate) and $C_6H_{12}N_4$ (HMT) precursors as this system has been studied

extensively and is known to promote the growth of ZnO one-dimensional structures. The chemicals were obtained from VWR and used as received.

Sample Preparation

Silk Solution

Silk cocoons were obtained from B. mori silkworms raised on a diet of Silkworm Chow (Mulberry Farms, Fallbrook, CA). Upon completion of the cocoons, the live pupae were extracted in order to avoid potential contamination or degradation of the fibroin protein.

Sericin proteins were removed from the fibers following the procedure outlined by Yamada et al [80]. Silk cocoons were soaked at 3.3% (w/v) in a solution of 8M Urea containing 40mM Tris-SO_4 and 0.5 M β-mercaptoethanol. The solution was heated to 90°C for 1 hr in a water bath. The silk fibers were stirred regularly to ensure complete removal of sericin proteins. The silk fibers were then removed and dried by centrifugation at 4000 RPM in a 50 ml tube. The fibers were then washed extensively with ultrapure distilled water (18 MΩ·cm) and again dried by centrifugation. The washing procedure was repeated five times to ensure complete removal trace urea and sericin from the fibers. The fibers were then lyophilized for 48 to 72 hours for removal of any residual water.

The dried silk fibers were processed further in the lab at Georgia Tech. Dried silk fibers were subsequently dissolved in a 50 ml tube containing 9.3M lithium bromide solution. The tube was placed in a hot water bath for one hour to achieve complete

dissolution. The solution was centrifuged to remove impurities. The solution was then dialyzed against distilled water using Slide-a-Lyzer dialysis cassettes (MWCO 3,500, Pierce) at room temperature for 2 days to remove the salt. Ultrapure distilled water was used to dilute the aqueous solution to the desired working condition of 0.2%-0.5% for thin film fabrication.

Silk and Polymer Films

Silicon substrates were cut into pieces of 12 by 15 mm and 2.5 by 2.5 mm (Figure 13). The substrates were then cleaned by using CTAB surfactant and then by exposure to a "piranha" solution according to usual procedure described in detail in elsewhere [[81, 82]]. Polymers were dissolved in DI water at the following concentrations: PS 2%, PAH 0.2%, PSS 0.2%, PAA 0.2%, silk 0.2%-0.6%. Films were created by typical LbL spin casting as described elsewhere [83, 84] onto a smooth silicon wafer using a PM101DT-R485 spinner (Headway Research, Inc., Garland, TX) at the speed of 4000 RPM. The films were then rinsed with water and spun dry. Silk was rinsed with a 1:1 solution of methanol/water.

Growth of Zinc Oxide Rods Using Peptide

The zinc oxide selectively binding peptide with sequence GLHVMHKVAPPRGGGC referred to hereafter as "ZnO1", was received from New England Peptide Co. and used without modification. The dry peptide powder was put into water and used at a concentration of 10mg/ml. For initial investigation of peptide on surfaces, 10µl of ZnO1 solution was drop cast on a polymer film and allowed to dry

completely in ambient conditions. Typically, the peptide layer thickness was ~4 nm depending on spin speed and humidity. The polymer films for these experiments were cast on a 12 by 15 cm silicon wafer (Figure 13).

Second, for investigation of vertical zinc oxide rods as there was a diminished supply of ZnO1, 5µl was dropped on a 2.5 by 2.5 mm polymer film so that the drop covered the entire surface (Figure 14). Peptide was not dried immediately however; after various times from one minute to one hour to allow adsorption of the peptide to the surface via hydrophobic interactions, the sample was spun dry at 4000 rpm. To prevent evaporation of the peptide, the sample was placed in a covered plastic dish and draped in wet paper towels.

The large silicon wafers were placed in a 20ml glass vial immediately after 5ml each of HMT and zinc nitrate were added and mixed in the vial (Figure 15). The small samples were placed in small 1.5ml plastic microcentrifuge vials filled with 0.5ml of each precursor. Samples were allowed to rest at the bottom of the vial. The small samples were later floated at the air-liquid interface in a large vial to avoid precipitates from solution falling on the surface.

An overview of sample preparation and ZnO growth can be seen in Scheme 1.

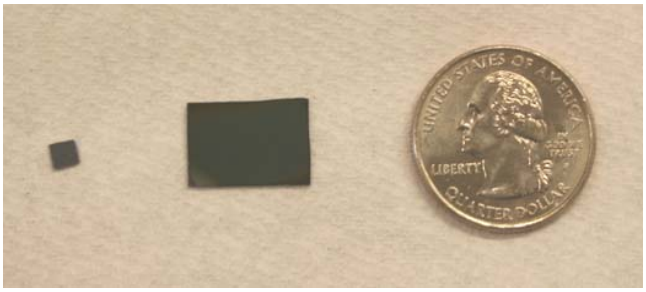

Figure 13. Small and large silicon wafer specimens

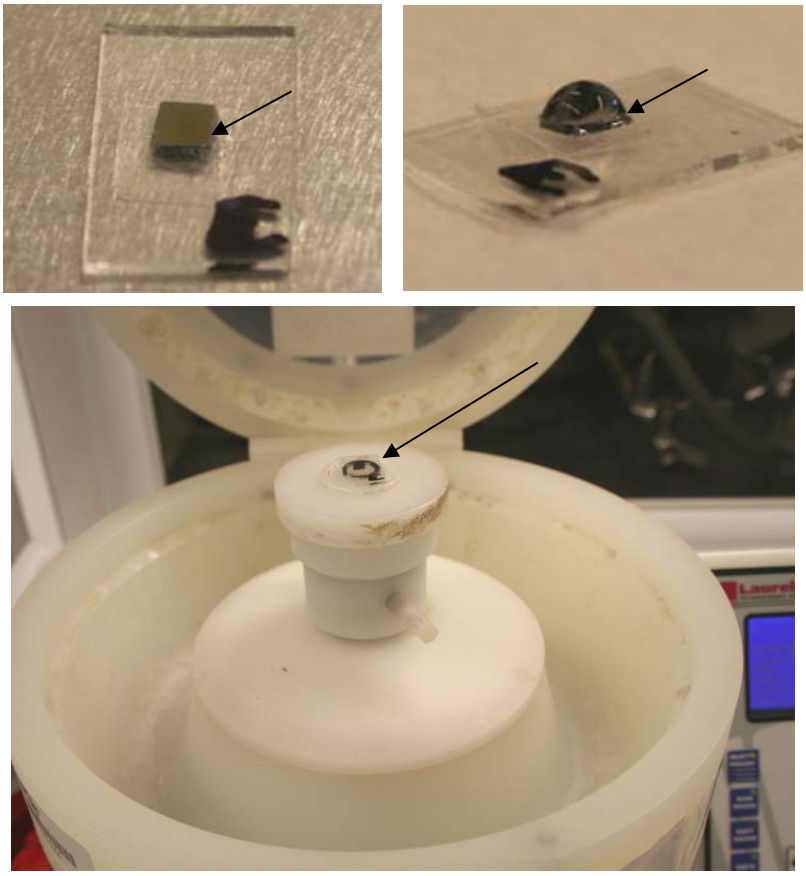

Figure 14. Small silicon wafer (arrow) mounted on a piece of glass for spin casting (top left), same small silicon wafer with peptide drop covering the entire surface (top right), and the same sample placed in the spin coater (bottom)

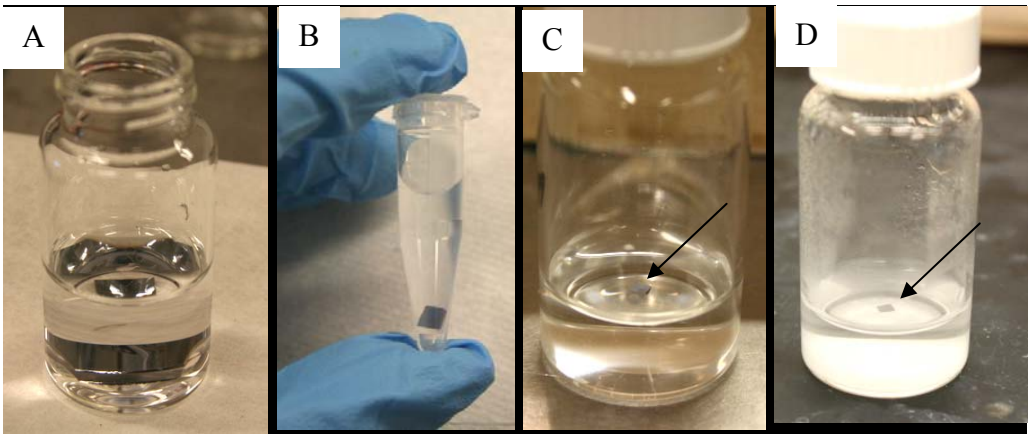

Figure 15. Sample placement in HMT/zinc nitrate for ZnO growth of large sample in 20ml glass vial (A), small sample in 1.5ml plastic vial , and small sample floating in 20ml glass vial before (C) and after (D) ZnO growth

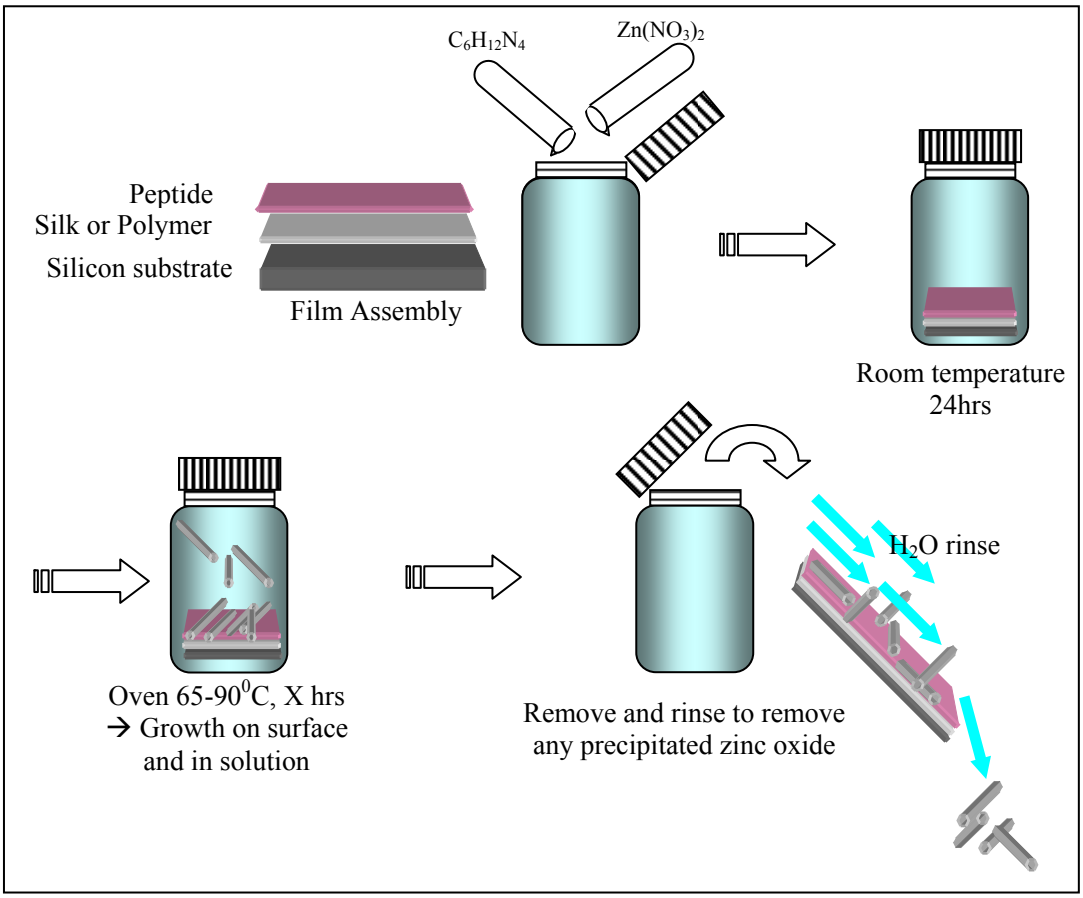

Scheme 1. Sample film assembly and growth of zinc oxide rods [85]

After growth of nanorods, in some cases surface density was calculated. Adobe Photoshop was used to create a 2D black and white image. Noise was removed with the median function which averages neighboring pixels as seen below in Figure 16.

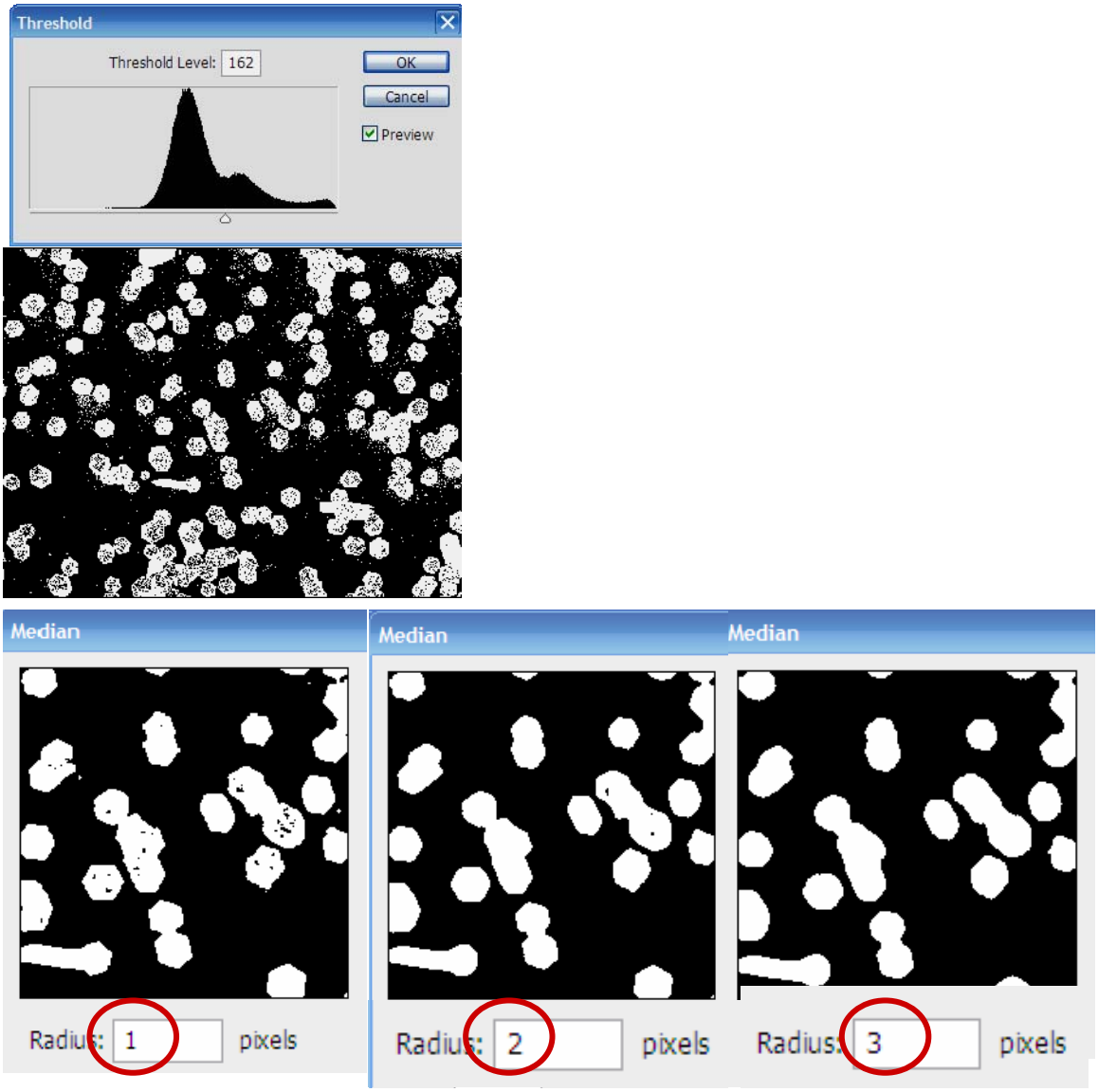

Figure 16. Process of analyzing a sample's surface coverage by setting a threshold and removing noise

Gold Nanoparticle Growth Using Silk

To investigate nanoparticles formation within the silk film, freely suspended films were fabricated as described elsewhere [86] by depositing a silk layer on top of a twenty bilayers of (PAH+PSS) on top of a sacrificial cellulose acetate (CA) layer. The sacrificial layer was spin cast on the silicon wafer from 2% acetone solution. The silk film was spun on top of twenty bilayers and then placed in between ten bilayers as seen in Scheme 3. Each layer was rinsed two times with water and spun dry.

To form gold nanoparticles, the CA+$(PAH+PSS)_{20}$+silk layered assembly on silicon wafers was immersed in a glass vial containing 15ml of $HAuCl_4$ as seen in Scheme 2. Various concentrations and soak times were used. The samples were then removed and rinsed lightly with a flowing stream of Nanopure water. Samples were dried under nitrogen. To analyze with TEM, the films were placed on 200 mesh copper grids.

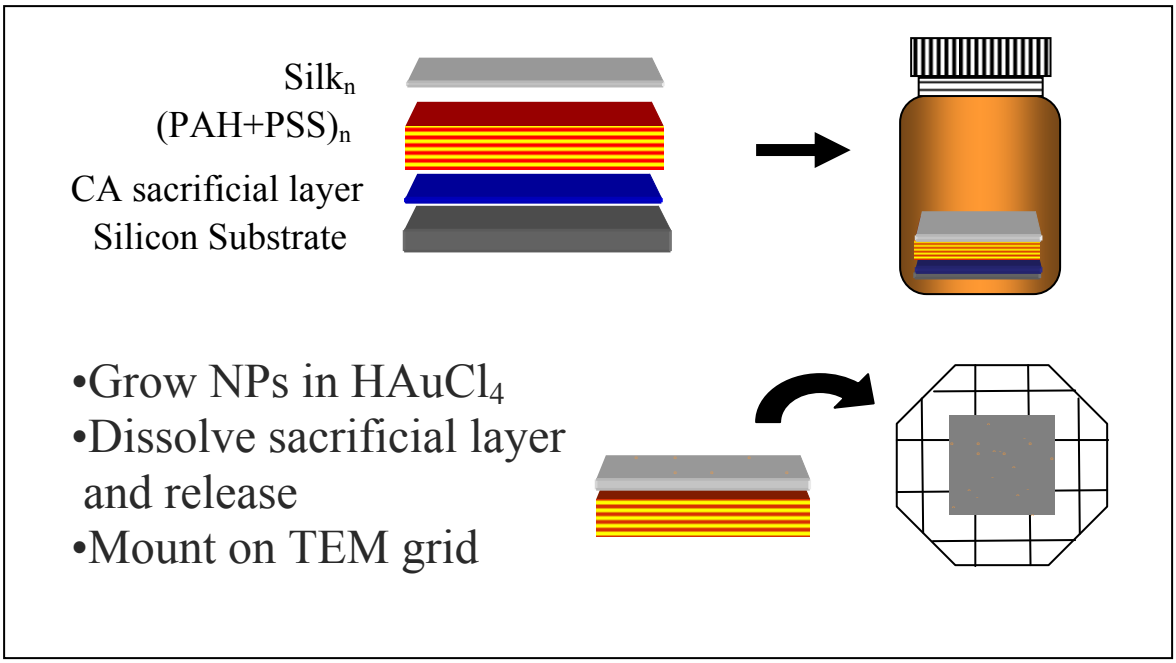

Scheme 2. Growth of Au NPs using a silk film and mounting for TEM analysis

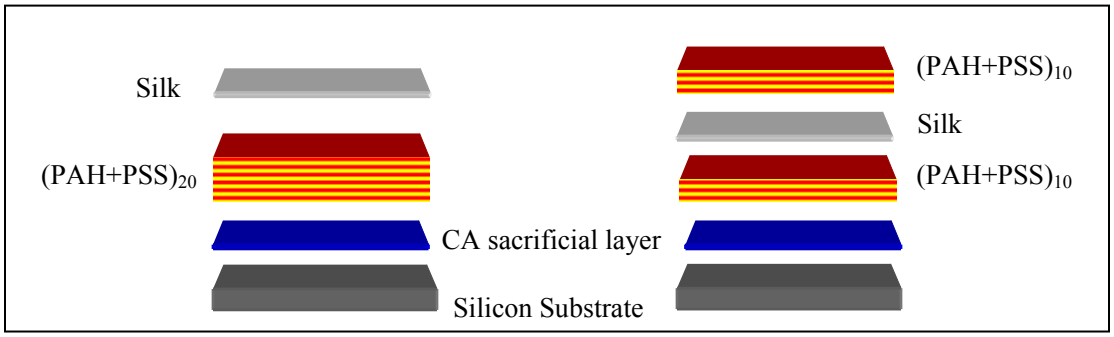

Scheme 3. Film assembly for gold nanoparticle growth using silk templates

Sample Characterization

Morphology and surface roughness of the polymer, silk, and peptide films were investigated with a Dimension 3000 atomic force microscope (AFM) (Digital Instruments) in the tapping mode. The AFM imaging in concurrent topography and phase modes was performed in the regime of the "light" tapping to avoid damaging the films [87].

The thickness of the films was obtained with a Woolam M-2000 ellipsometer. Values were collected at incident angles of 65˚, 70˚, and 75˚. Contact angle was taken using a KSV contact angle instrument.

SEM images of zinc oxide were done on LEO 1550 and 1530 thermally assisted field emission scanning electron microscopes (SEM) at 5kV. Nanoparticle formation in silk was analyzed with a JEOL 100CX transition electron microscope (TEM) operating at 100kV. Both SEM and TEM were done at the Georgia Tech Center for Nanostructure Characterization.

CHAPTER 3

RESULTS AND DISCUSSION

In this chapter, the ability for silk films to biomineralize gold nanoparticles will be investigated. Secondly, a zinc oxide selectively binding peptide will be used as a film on silk and other polymer surfaces to control the formation of zinc oxide. Finally, the synthesis of vertical zinc oxide rod arrays on completely organic templates will be discussed, including control over rod size and surface density.

Gold Nanoparticle Synthesis Using Silk Films

Silk can form a film by sequentially spin coating layers onto a substrate [35]. Using a 0.2wt% solution of silk in water, layers were built up by spin coating a silk layer and rinsing with water between each layer at 3600rpm. A linear relationship between layer number and thickness of the film is shown in Figure 17 below. The "zero" layer thickness represents the underlying SiO_2, the cellulose acetate sacrificial layer, and the polyelectrolyte bilayers upon which the silk film was cast. Each layer in this experiment had a thickness of 3nm ±0.3 nm. The thickness determined from applying a linear fit to the graphed data was 3nm (R^2 = 0.9968). The sacrificial layer of cellulose acetate deposited before the silk was 94.65nm.

Results for multiple samples consistently exhibit a linear relationship between layer number and film thickness. Exact thickness values were difficult to reproduce because of variations in each silk batch but a linear relationship was consistently

demonstrated. Thickness was found to be extremely dependent on experimental conditions. To achieve identically thick layers, the following conditions had to be constant: batch and concentration of silk, rinse solution (water or water + methanol mix), spin coater spin speed, room temperature, and room humidity. A silk film thickness of 60+ nm was robust enough to exist as a freestanding film.

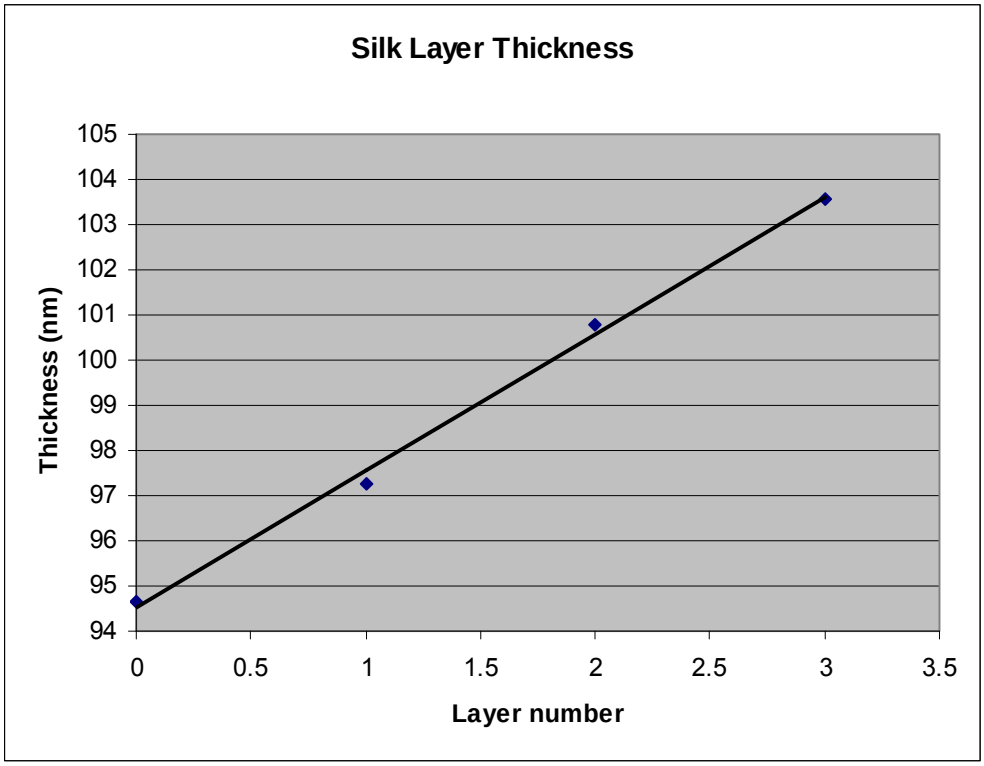

Figure 17. Silk layer number compared with total film thickness, resulting in a linear relationship.

In many studies, silk fibers have been used to reduce gold from solution, many times with the aid of a reduction agent such as sodium borohydride. Regenerated thin films had never been investigated for potential metal reduction capabilities.

In the first experiment, a substrate-supported film of silk was used and exposed to gold chloride to investigate any reduction. Five polyelectrolyte bilayers of $(PAH+PSS)_5$ were built on a sacrificial layer of cellulose acetate (spun from a 2wt% p-dioxane solution) on a silicon substrate. Five layers of silk were then spun on top of the bilayers, each rinsed with a 1:1 water/methanol mix. Gold chloride at approximately 1M concentration was then dropped on top of the horizontal sample to completely cover the surface. After two hours, the sample was then dried and rinsed with water. No reducing agent (i.e., sodium borohydride) was used. The $(PAH+PSS)_5$ + $silk_5$ film was released from the substrate with acetone and placed on a copper TEM grid for analysis. The film turned out to be barely robust enough to be free standing and only one area was transferred and analyzed successfully.

Surprisingly, fairly monodisperse nanoparticles 5-8nm in diameter were formed. Figure 18 shows two different TEM image magnifications. The nanoparticles were evenly spaced over the area of the suspended film and fairly monodisperse.

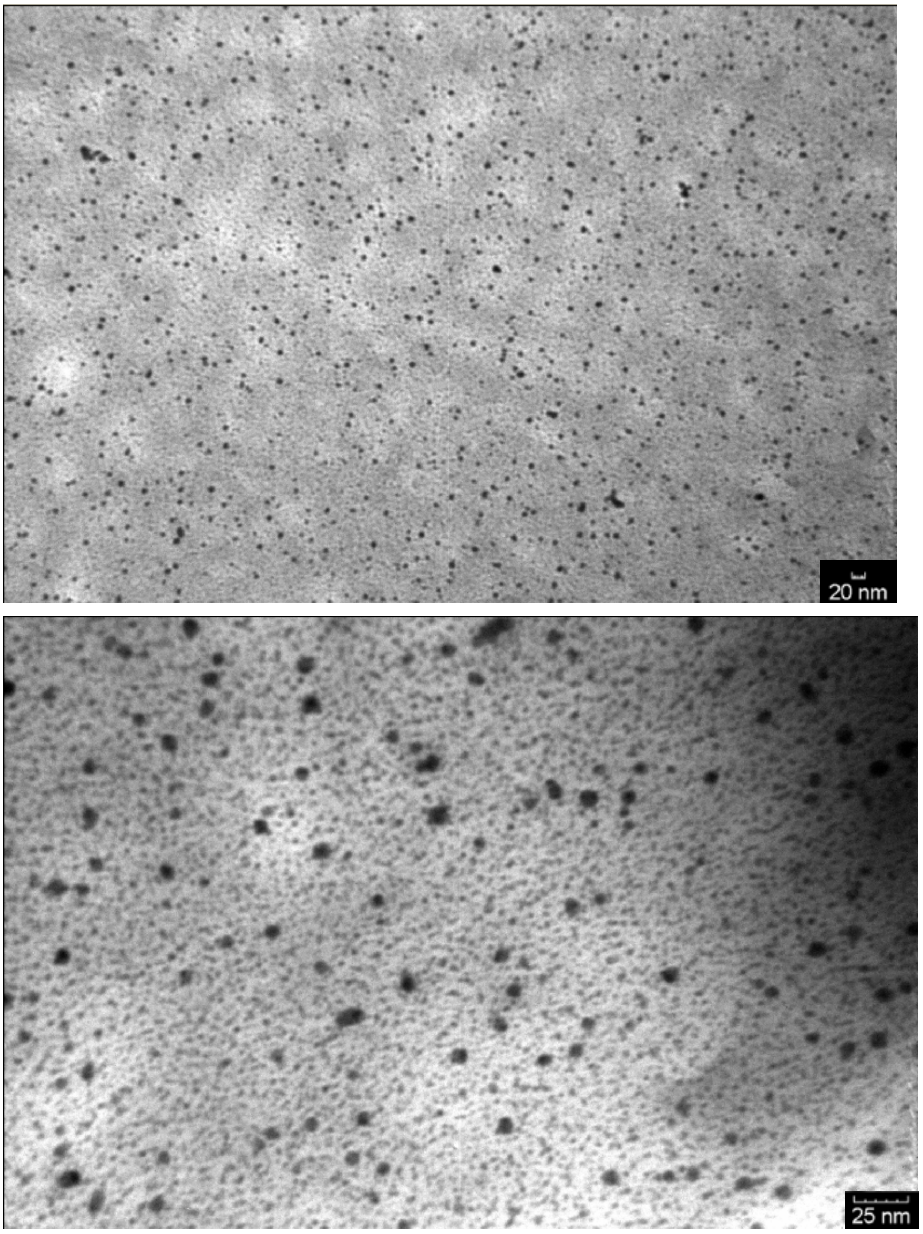

Figure 18. Gold nanoparticles formed after exposing $(PAH+PSS)_5+silk_5$ film on silicon substrate to 0.1M $HAuCl_4$ for 2 hours

To investigate further, a set of samples were completely submerged in vials of 1.6mM gold chloride for 22hrs before being removed and rinsed gently with water. Samples included both substrate-supported films and freely suspended films, which were prepared by placing the film on a TEM prior to exposure. Twenty bilayers of (PAH+PSS) were used under the silk films to ensure strength for TEM analysis.

Using the lower concentration of 1.6mM and longer soak time of 22hrs, large particles of different shapes including triangles, pentagons, hexagons, and spherical like shapes were observed in addition to smaller nanoparticles 5-10 nm as seen in Figure 19. The smaller particles are similar to those in Figure 18. The density of nanoparticles across the sample was fairly sparse and uneven.

Interestingly, the density of growth was increased when the film was in a freely suspended state prior to gold chloride exposure as seen in Figure 20. The nanoparticles were still various shapes but generally were smaller, 27-40nm, than those grown on the silicon substrate in Figure 19.

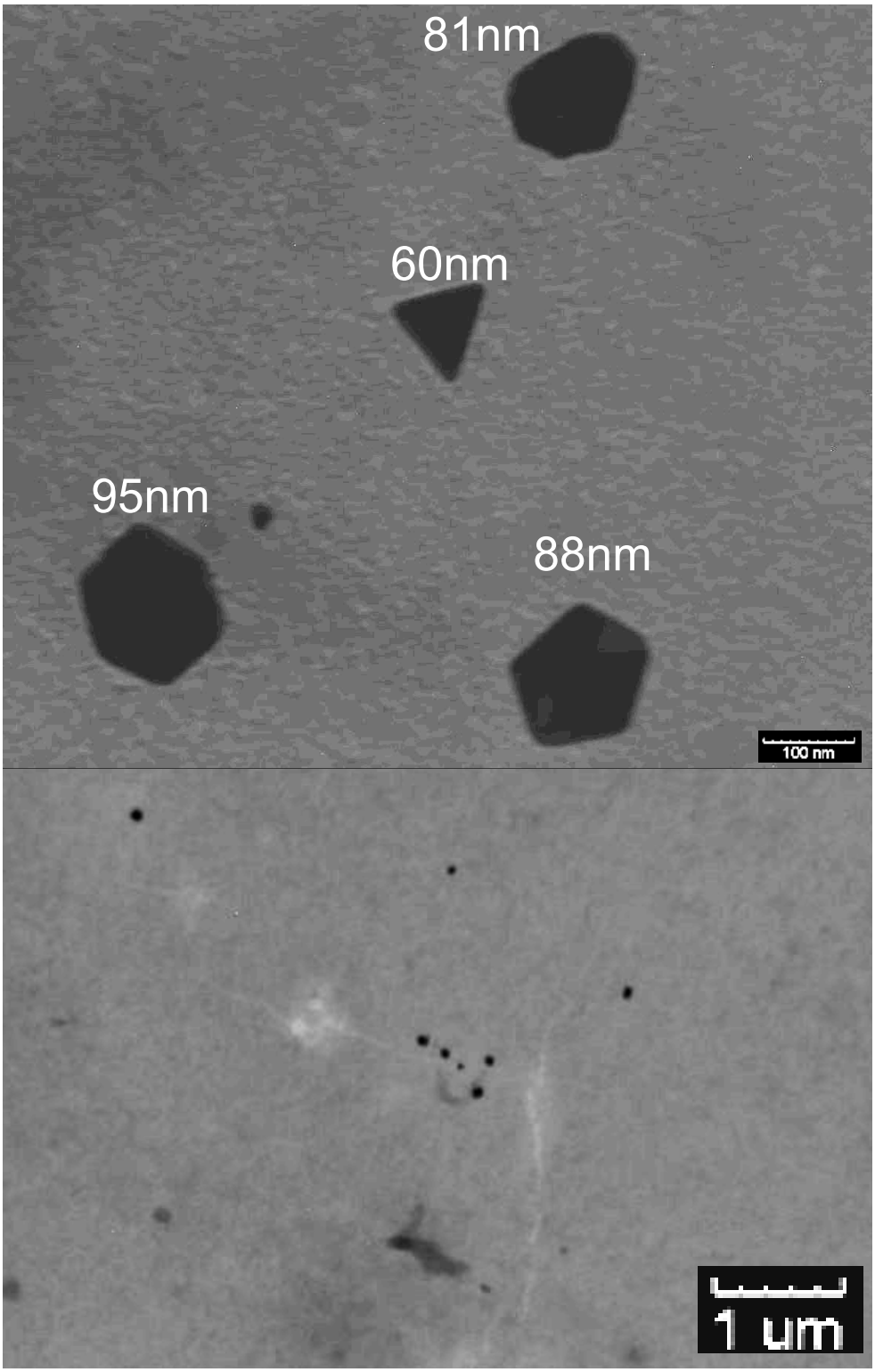

Figure 19. $(PAH+PSS)_{20}$+silk on a silicon substrate exposed to 1.6mM $HAuCl_4$ for 22 hrs.

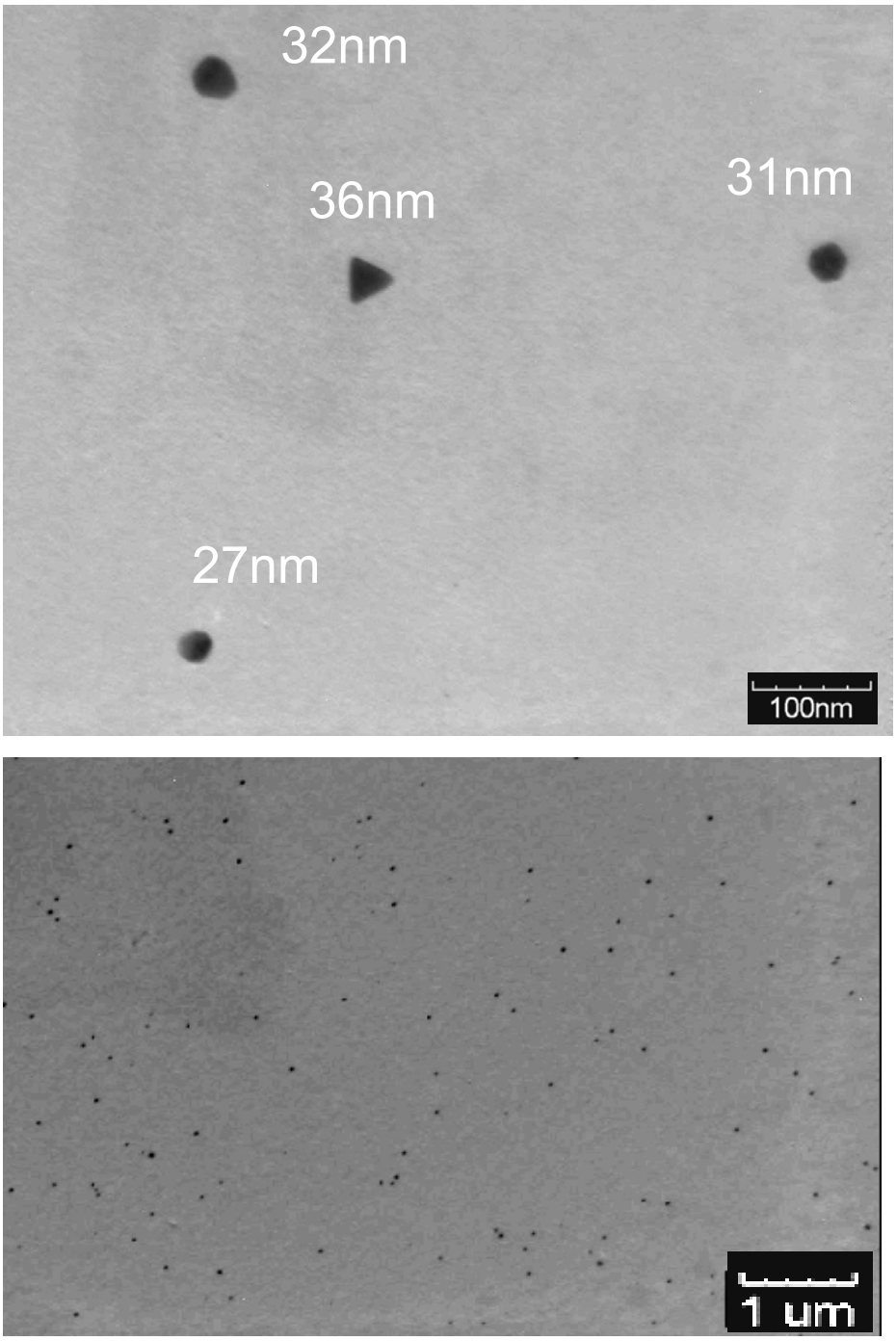

Figure 20. $(PAH+PSS)_{20}$+silk film suspended on a TEM grid exposed to 1.6mM $HAuCl_4$ for 22 hrs

A sample with an embedded silk layer was built to investigate the possible formation of gold nanoparticles at a specific place within a thin film. The LbL assembly included ten polyelectrolyte bilayers on either side of the silk film, $(PAH+PSS)_{10}$+silk+$(PAH+PSS)_{10}$. Again, the samples were exposed to 1.6mM gold chloride for 22 hrs, removed and rinsed with water before drying under a flow of nitrogen. Large shapes with various geometries were surrounded by numerous small nanoparticles <10nm in diameter as seen in Figure 21. The result here is similar to the freely suspended $(PAH+PSS)_{20}$+silk film in that fairly disperse, dense nanoparticles <10nms are seen on the sample along with larger shapes with both asymmetrical and symmetrical geometries, commonly three to six edged shapes. Gold is a close packed cubic structure and can form spherical, triangular, square and hexagonal shapes easily; research has shown properties of these nanoparticles are extremely dependent on size and shape such as light scattering properties [88].

The results presented here indicate that gold nanoparticles can successfully be synthesized, at room temperature with some control over density and size using a thin silk film. In addition, the silk film can be embedded between polyelectrolyte bilayers and still participate in biomineralization. This method provides a one-step room temperature method for the formation of fairly monodisperse gold nanoparticles. Further investigation is needed to understand the range of control over density and size. The control over size is extremely important as gold nanoparticles have very diverse properties depending on the material's size.

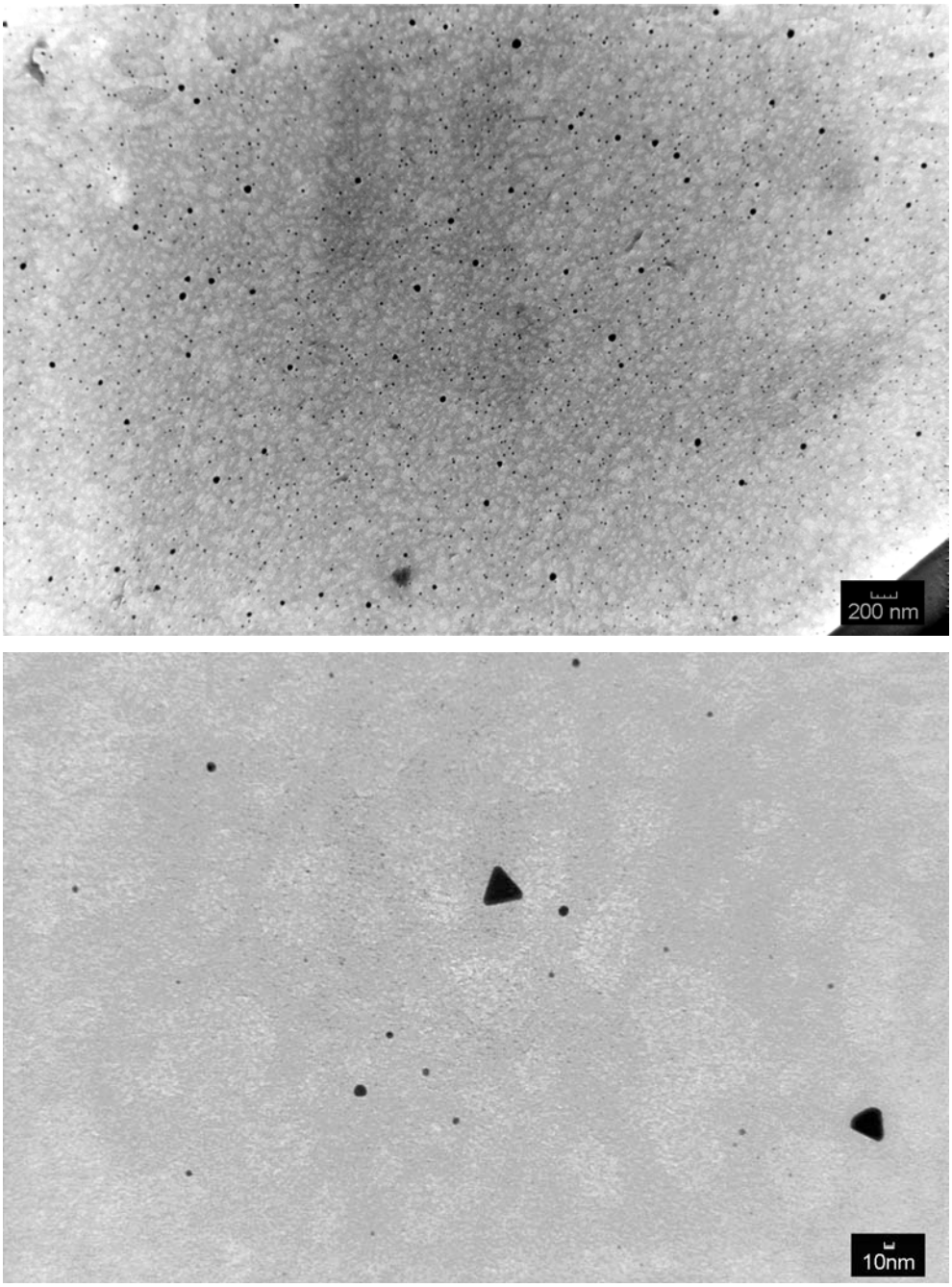

Figure 21. Film of $(PAH+PSS)_{10}$+silk+$(PAH+PSS)_{10}$ freely suspended and exposed to 1.6mM $HAuCl_4$ for 22 hrs.

ZnO1 Peptide Structure and Properties

This zinc oxide selectively binding peptide was identified using the phage display technique and supplied by scientists at Wright-Patterson Air Force Base.

The ZnO1 peptide is a 12 amino acid peptide sequence with a –GGGC end. The peptide sequence as received, using one letter amino acid abbreviations, is as follows:

H_2N-GLHVMHKVAPPRGGGC-OH

In another popular form using three letter abbreviations, the peptide is described as follows:

H_2N - Gly Leu His Val Met His Lys Val Ala Pro Pro Arg Gly Gly Gly Cys – OH

Amino acids all contain an NH_2 group, known as the amino group, and a carboxyl group. To create chains of amino acids, a condensation reaction occurs and peptide bonds link amino acid "residues." The protein's mass is 1616 Da.

Each amino acid can have a charge and thus, a protein can have an overall charge. The charge of an amino acid is dependent however upon pH. An isoelectric point (pI) of a protein describes the point at which it has no net charge. Below this point, proteins carry a positive charge and subsequently, above the pI they have a net negative charge. The isoelectric point of a peptide is important because it can help in predicting how it will behave in solution or on different substrates, at a certain pH.

Using the bisection method for determining protein's isoelectric point and calculation using a program from Lukasz Kozlowski [89], the isoelectric point for ZnO1 is determined to be 9.51. Different methods for determining pK values for each amino acid can result in disagreements of pI values. Using other methods with various pK values, the isoelectric point of ZnO1 is calculated as 9.5 ± 0.5 [90]. When used at neutral pH around 7, ZnO1 should behave with a positive net charge. It is important to note however that a folded protein can exhibit different behavior than an isoelectric point will predict, as pI uses pK values of isolated residues.

The chemical structure of ZnO1 and a molecular model cartoon are shown below in Figure 22, created with ChemDraw Pro and Figure 23, constructed using Material Studio software.

Hydrophobicity plot (Figure 24) using the Kyle-Doolittle scale was constructed using software available from R. A Bowen [91]. The 16 amino acids of ZnO1 are represented from left to right in the plot as displayed in Figure 22 and Figure 23. Regions above the "0" line are hydrophobic in character. The left side of the plot suggests a hydrophobic end region, potentially available for hydrophobic surface interactions.

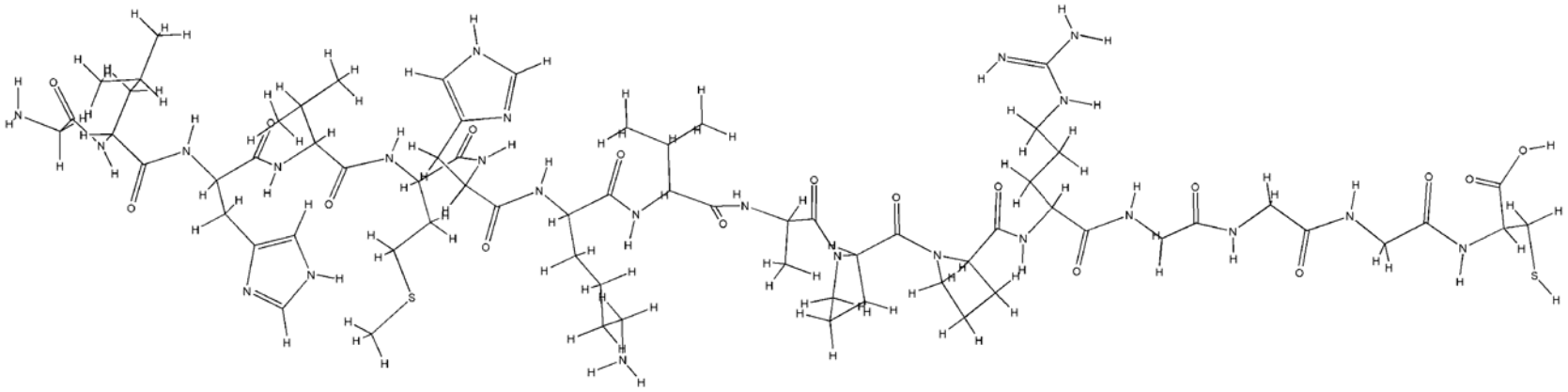

Figure 22. ZnO1 Chemical Structure GLHVMHKVAPPRGGGC

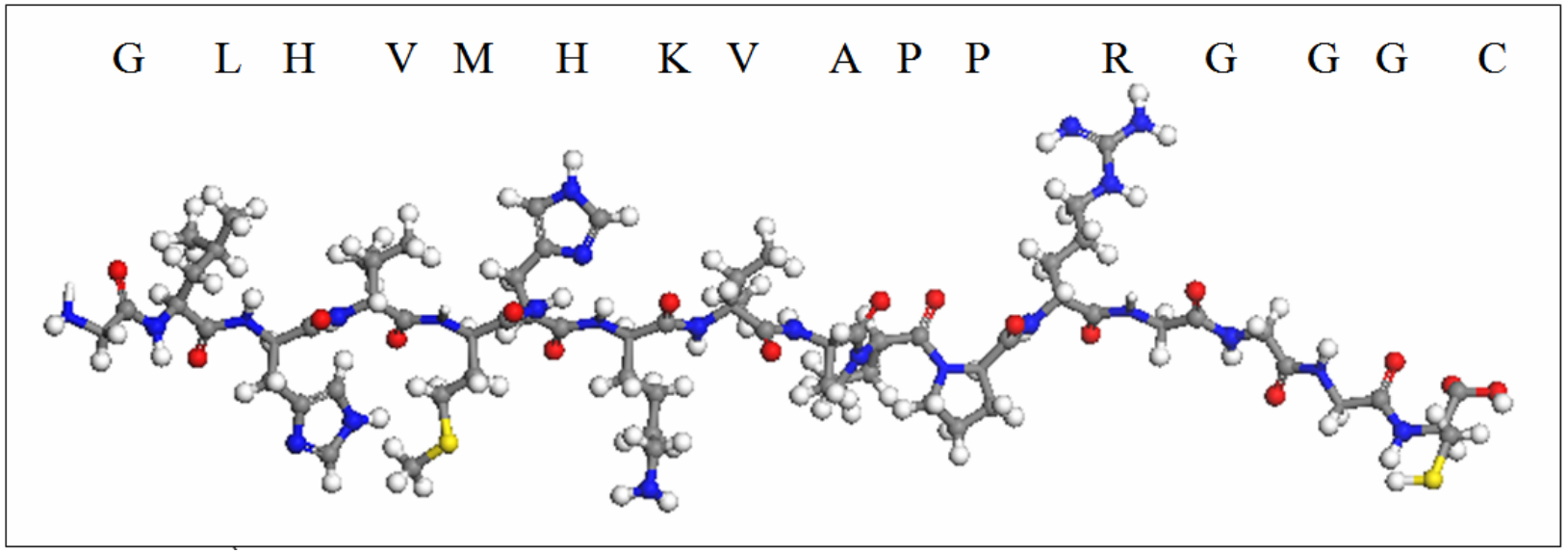

Figure 23. Model of ZnO1 peptide with sequence H2N-GLHVMHKVAPPRGGGC-OH

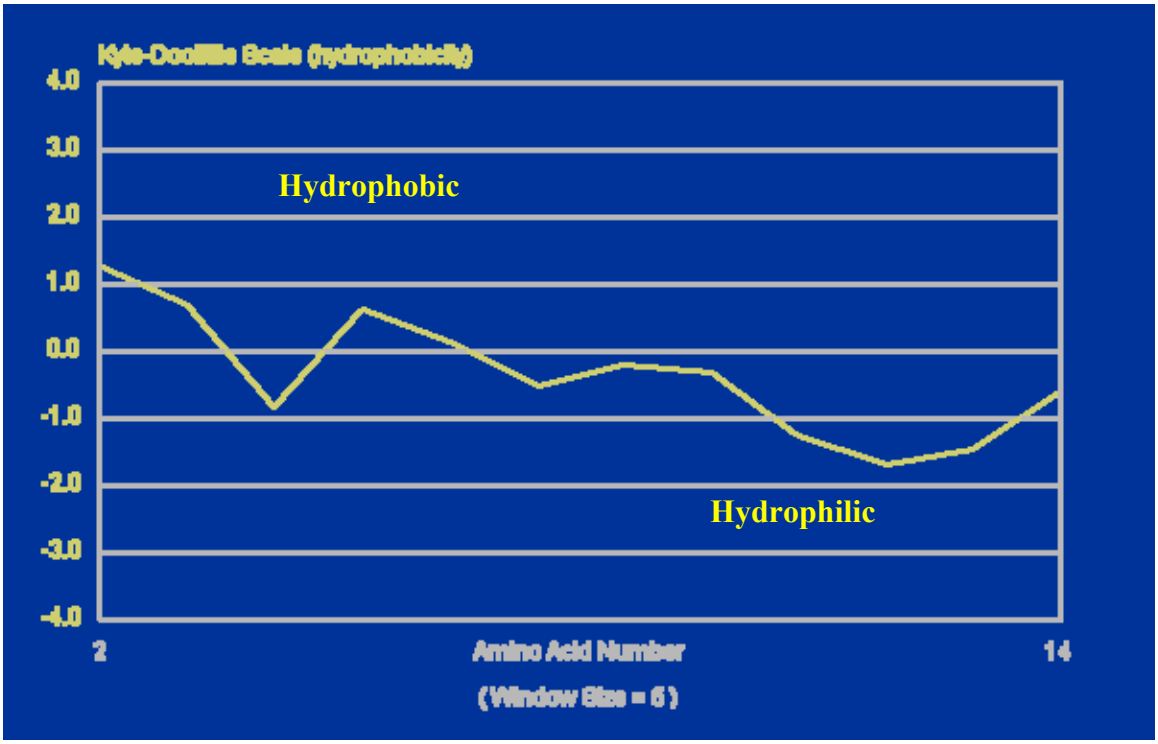

Figure 24. Hydrophobicity plot for ZnO1 showing hydrophobic regions of the sequence on the left

Zinc Oxide Nanorod Growth Using Peptide on Organic Films

Experiments were conducted to determine the ability of ZnO1 to tether to a polymer surface and the subsequent effect on the growth of zinc oxide micro- and nanorods. Samples were prepared using a solution of ZnO1 peptide in water that was diluted to the desired concentration. The polymer surfaces were prepared spin coating solution onto a thin silicon wafer in usual layer-by-layer technique. The peptide was drop cast onto the polymer surface and allowed to dry completely.

Growth on a Silk Film

Silk surfaces were prepared by repetitively spin coating 0.2% aqueous solution onto a 12mm x 15mm clean silicon wafer at 3500rpm to build up a silk film. After ZnO1 (5mg/ml) deposition, the samples were placed in a zinc nitrate/HMT 1:1 solution. Several growth parameters were varied including oven temperature, time in oven, and zinc nitrate and HMT concentration.

Initial experiments tested the growth of zinc oxide under various conditions on samples with peptide and on samples without. The initial conditions kept the samples at room temperature (RT) for 24hrs and then in the oven at 65°C. The samples were films of nine silk layers with a thickness of ~6nm per layer, totaling on average ~55nm. After deposition of ZnO1 and exposure to a zinc nitrate/HMT 1:1 solution (both 0.1M concentrations), the samples with newly formed zinc oxide on the surface were removed from solution and rinsed lightly with water. This rinsing removes all non-adhered rods, which form in solution and can be collected while removing the sample from solution.

SEM analysis in Figure 25 shows the difference in growth on a silk surface in the presence of peptide and without. Growth was achieved in both conditions in the silk system. In Figure 25, the density difference in the presence of peptide (Figure 25A) compared with the sample in which no peptide was present (Figure 25B) is significant and repeatable. Coverage of zinc oxide structures on the silk film was uniform when peptide was present, in contrast to the sporadic growth and aggregation seen in the control sample.

Surface density coverage was calculated using five different areas on each sample, imaged and analyzed using Adobe Photoshop. After setting a threshold clearly separating the nanorods (seen as white areas) with the background (black), the percentage of white pixels on the image was obtained and reported as the percentage of nanorod surface coverage. Noise was removed using the surrounding pixel median function, set to one or two pixels. The degree of vertical orientation of the rods was not accounted for when analyzing the projected coverage on a 2D surface image. Two assumptions were made in this analysis. First, that the vertical orientation was random and similar for all samples and thus was not accounted for. Second, the pixel median function did not substantially affect the analysis. As samples with more rods have consequently more edges, the effect of setting a threshold and averaging surrounding pixels to eliminate noise could potentially be more substantial and skew analysis of smaller rods or more dense surfaces.

For the samples illustrated in Figure 25A and B, the coverage was 18.3±1.8% with 301 rods and 7.2±3.6% with 87 rods respectively after averaging the coverage from 5 images. Rods were counted on images of 500x magnification. Summarized in Figure 25. Zinc oxide rods formed on silk films A) in the presence and B) in the absence of ZnO1 after exposure to Zn(NO3)2 + HMT 1:1 bath , both at 0.1M for 24hrs at room temperature followed by 24hrs at 65˚C.

Table 3, after counting the number of nanorods present (1) and dividing the total area of the surface covered by nanorods (2) with the number of nanorods, the area per nanorod (3) was 0.06% for A (with ZnO1) and 0.08% for B (without ZnO1). Lengths of rods ranged from 8.5-9 μm and widths 2.3-4 μm.

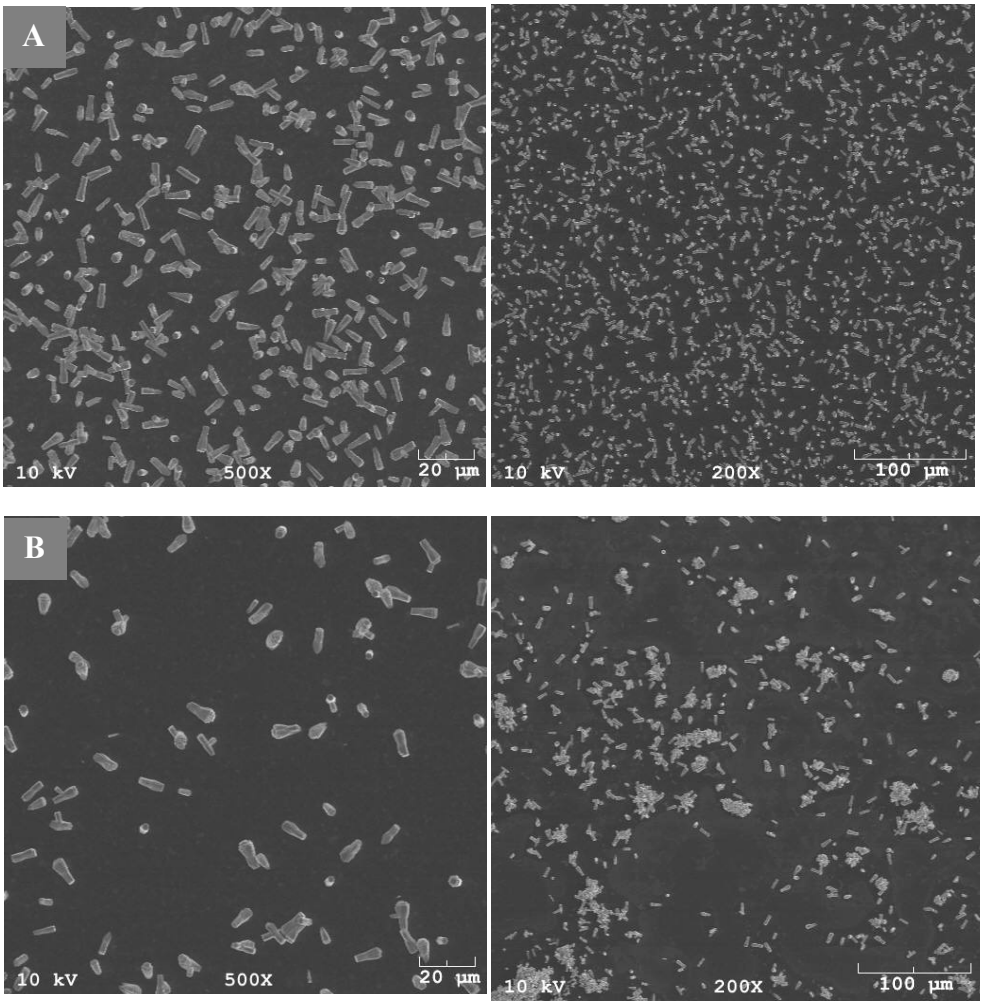

Figure 25. Zinc oxide rods formed on silk films A) in the presence and B) in the absence of ZnO1 after exposure to $Zn(NO_3)_2$ + HMT 1:1 bath , both at 0.1M for 24hrs at room temperature followed by 24hrs at 65°C.

Table 3. Difference in rod size in the presence and absence of ZnO1 peptide. Samples were held at RT for 24hrs and 65°C for 24hrs, $Zn(NO_3)_2$ and HMT were kept at a 1:1 ratio of 0.1M concentration

0.1M *RT 24hr, 65°C 24hr*	(1) Average # of rods	(2) Surface covered	(3) = (2) / (1) Surface per rod
ZnO1 peptide	323±22	18.3%	0.06%
No peptide	87±5	7.2%	0.08%

It is worth noting that although much work has illustrated the effect on structure of ZnO grown in solution with the same zinc nitrate/HMT system used here [92], there is no observable, within statistical significance, difference in structure or c-axis length in the presence versus the absence of peptide. It can be concluded that there are negligible amounts of peptide desorbing from the surface and/or present in solution during ZnO growth for these experiments.

Controlling Size and Density of Zinc Oxide on Silk

Various parameters such as time, temperature, and zinc nitrate/HMT concentrations were changed to determine the tunability of zinc oxide growth. These effects will be described.

First, the silk films were rinsed with either water or a water/methanol 1:1 mix before depositing peptide and ZnO growth. No difference was observed. For the rest of the experiments presented here, a 1:1 water/methanol rinse was used on the silk layers.

Secondly, 1 and 9 layers of silk were put on silicon wafers and then peptide drop cast on each. There was no difference in ZnO growth based on silk layers. In further experiments with zinc oxide, 1 layer of silk was used to preserve material.

To analyze the effect of time in the oven, samples were prepared as in previous description. The growth conditions were identical to those in Figure 25 except growth was stopped after a 65°C oven time of 2 hours. Substantially smaller nanorods were grown in the presence of peptide as seen in Figure 26. Nanorods were not uniform and ranged from 50-200 nm in diameter and 190-500nm in length. Without peptide, the silk surface had very few nanorods; the majority was in large aggregates. However, this did indicate that the nucleation effect of peptide on a surface at the microscale was similar when reduced to the nanoscale.

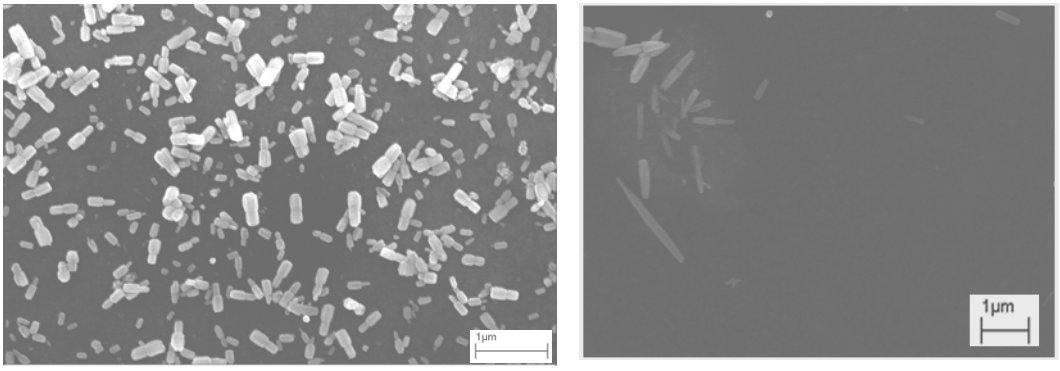

Figure 26. ZnO grown after 24hrs at RT and then 2hrs at 65°C on silk plus ZnO1 (left) and on silk (right) in 0.1M of zinc nitrate/HMT 1:1

Next, temperature was changed to 90°C. Samples were exposed to the zinc nitrate/HMT bath, at different molar concentrations for 24hrs at room temperature and then 90°C for 4 hrs.

Under these conditions, rods grew over the entire surface whether peptide was present or not, eliminating any discernable effects. Figure 27 shows the full surface

growth of zinc oxide on a silk + peptide surface (A) and a silk control sample (B) after 4hrs at 90°C. Dense, bundled, uncontrolled growth occurred on both samples at the elevated temperature.

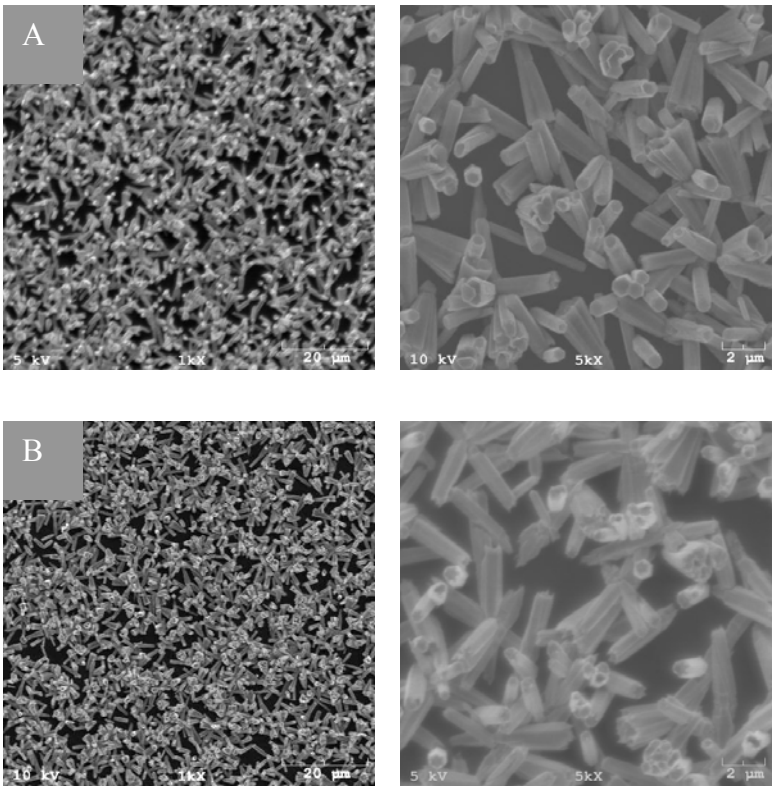

Figure 27. ZnO after 24hrs RT and 90° 4hrs in 0.1M zinc nitrate / HMT 1:1 solution on silk (B) and on silk with peptide drop cast (A)

It is evident in the literature and here that with the zinc nitrate/HMT system, temperature and time highly effect the zinc oxide nanorod growth. The effect of peptide is only observable under certain conditions when a system facilitates growth, as in the silk system. For investigation of peptide in a silk/ZnO system, the conditions have to be such that formation is controlled and not overly abundant in the control sample.

Using a temperature of 90˚C, different concentrations of zinc nitrate and HMT were used while keeping them at a 1:1 ratio. Figure 27 shows 0.1M concentrations. After 4hrs, significantly less growth was achieved by reducing the concentration to 0.01M and further to 0.001M. Figure 28 shows the decrease in rods from dropping the concentration to 0.01M. The results of peptide presence under these conditions are reminiscent of the 65˚C, 24hr growth in Figure 26 where spatial density was controlled and uniform across the surface.

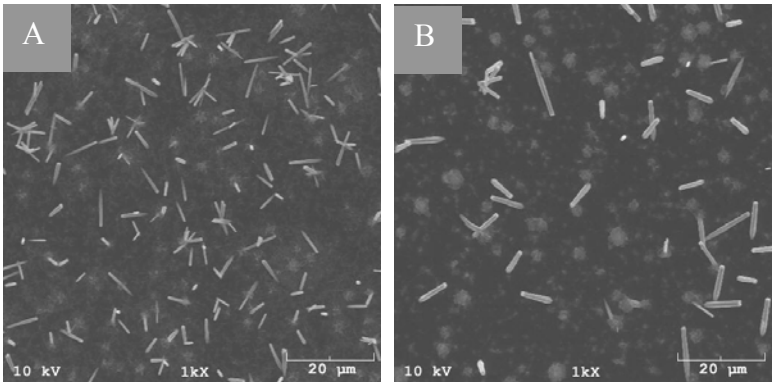

Figure 28. ZnO after 24hrs RT and 4hrs 90° in 0.01M zinc nitrate / HMT 1:1 solution A) on silk with drop cast peptide and B) on silk

The percentage of surface covered in the two cases of Figure 28 was not statistically different as summarized in Table 4. However, there was a visible difference; the number of nanorods was significantly larger in A.

Table 5 shows the area per rod or size of the rod was smaller on average when using the peptide by a factor of 2.38, calculated by dividing the average surface area

covered in an image (2) by the number of nanorods in each image (1) and then comparing the calculated surface area per rod (3) values.

Table 4. Surface coverage density at different concentrations of $Zn(NO_3)_2$ and HMT. Samples were held at RT for 24hrs and 90°C for 4hrs, $Zn(NO_3)_2$ and HMT were kept at a 1:1 ratio.

RT 24hr, 90°C 4hr	0.1M	0.01M	0.001M
ZnO1 peptide	~100%	6.9 ±1.5%	<<1%
No peptide	~100%	5.5 ±1.3%	<<1%

Table 5. Difference in rod size in the presence and absence of ZnO1 peptide. Samples were held at RT for 24hrs and 90°C for 4hrs, $Zn(NO_3)_2$ and HMT were kept at a 1:1 ratio of 0.01M concentration.

0.01M *RT 24hr, 90°C 4hr*	(1) Average # of rods	(2) Surface covered	(3) = (2) / (1) Surface per rod
ZnO1 peptide	144±14	6.9%	0.05%
No peptide	48±4	5.5%	0.11%

To attempt reach nanoscale rod diameters at 90˚C, the HMT:zinc nitrate ratio was adjusted to 3:1 by using 0.1M and 0.033M solutions. After one hour at 90°C, rods of similar morphology as above were grown. The diameters were reduced to 100-200 nm.

It was determined that peptide facilitates uniform growth on the surface of silk and, in the examples described, peptide was shown to increase both surface coverage and rods on the surface while reducing size. The effect of peptide can be masked however, as was shown in the silk system by the film itself facilitating ZnO growth under certain

time, temperature, and solution concentration conditions. The growth in systems such as silk without peptide is shown to be uncontrolled, i.e., aggregation as in Figure 26B and rod size increases as in Figure 28B. As the peptide can dictate the nucleation of ZnO, the ability to control growth or pattern other polymer surfaces using ZnO1 could be possible.

The presence of peptide in general increases the amount of ZnO grown and decreases the size of rods. The density of rods on the surface an also be reduced by decreasing the molar concentration of HMT and zinc nitrate. It was also shown that the diameter could be reduced to the nanometer scale by reducing the time in the oven and possibly by reducing the ratio of zinc nitrate to HMT although that effect is still unclear.

Major difficulties during these experiments centered on the quantities available of both materials or lack thereof and the stability of aqueous silk. To address the issue of availability and stability of silk for further investigation, commercial polymers were investigated as replacement templates for ZnO1 deposition and subsequent ZnO growth. These polymers were selected as they are typically cast as films, either alone in the case of polystyrene or as polyelectrolyte bilayers as is the case for PAH, PSS, and PAA.

Typically, zinc oxide seed layers are used to control and increase the nucleation. It appears that ZnO1 facilitates the growth of zinc oxide on the surface in similar ways, as a nucleation site for rod formation. Using ZnO1 could allow the ability to control growth on a silk or other polymer surface without the use of an inflexible inorganic layer.

Growth of ZnO on Polymer Films

Polymers with a mixture of properties, including hydrophobicity and assorted polyelectrolytes were investigated to determine the role of peptide on different surfaces. Four common polymer surfaces were investigated, including PAH, PSS, PAA, and PS.

Polyelectrolyte bilayers were made by creating three bilayers using charged polymers and alternating the terminating top layer. Films with a PAH (+) surface were made by creating bilayers of $(PSS+PAH)_3$. Similarly, PSS (-) surfaces were assembled $(PAH+PSS)_3$ and PAA (-) films were assembled $(PAH+PAA)_3$.

On the surfaces of both strong polyelectrolytes PAH and PSS, growth was sparse and not significantly changed when peptide was present.

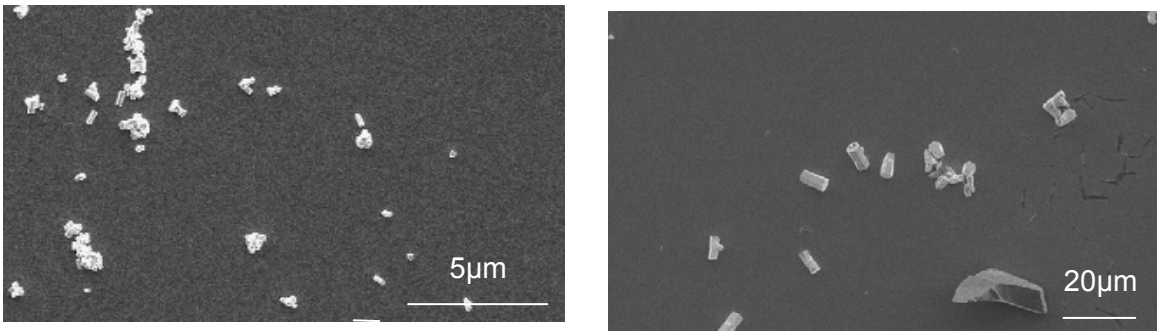

Figure 29. ZnO growth on polyelectrolyte surface PSS (left) and PAH (right)

PAA, a weak negatively charged polyelectrolyte, did exhibit a change in nanorod structure and density of rods across the surface. Interestingly, nanorods on a PAA surface were not complete and generally had a void where most nanorods will have a small twin boundary as seen in Figure 30 (left). Peptide did not have any effect on

growth, possibly because it was not deposited successfully on the PAA surface as seen in Figure 30 (right).

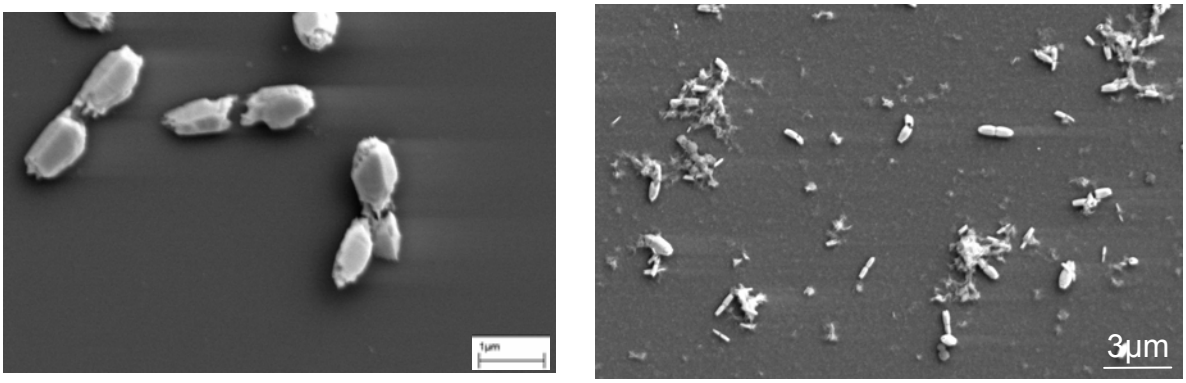

Figure 30. ZnO grown on PAA (left) and PAA with peptide (right)

Polystyrene, a neutral hydrophobic polymer, is known to be favorable for the adsorption of biomolecules via their hydrophobic domains, which are available for hydrophobic interactions. From the hydrophobicity plot in Figure 24, ZnO1 has a hydrophobic region on one end of the peptide. Here, ZnO uniform nanorods readily formed on a peptide coated surface of polystyrene as seen in Figure 31. The image on the right clearly shows where the peptide drop was deposited and growth occurred.

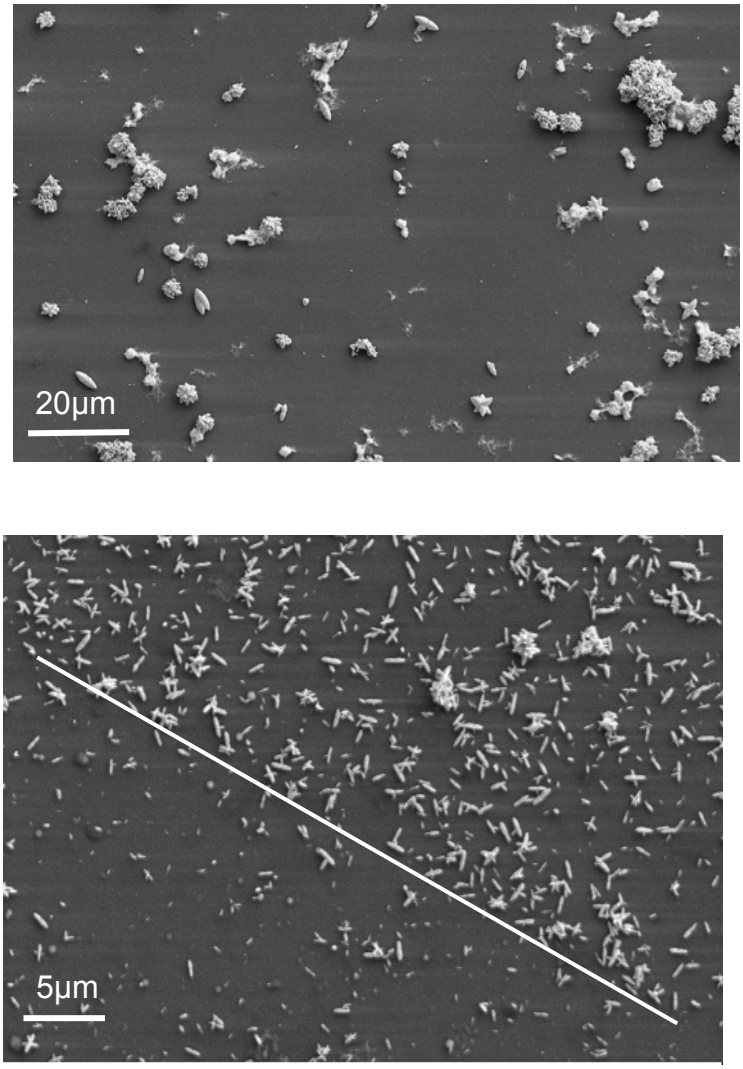

Figure 31. ZnO on polystyrene (top) and ZnO on polystyrene plus ZnO1 (bottom); the boundary where the peptide drop was cast and dried is clearly visible (bottom)

Insitu Growth of Zinc Oxide Within Silk Films

Preliminary results suggest that the ZnO1 peptide could dictate, to some extent, the nucleation of nanorods on a surface. To investigate this further, nine silk layers were topped with peptide at 10mg/ml, followed by another nine silk layers built on top of the

peptide to form a film of $silk_9$+ZnO1+$silk_9$ as seen in Scheme 4. Nine layers of silk had a thickness of ~50nm. ZnO was grown as in Scheme 1. 0.1M zinc nitrate and HMT were mixed at a 1:1 ratio and samples were submerged in the vial for 24hrs at RT and 65°C for four hours. Growth was present in the embedded layers although less dense than those formed on a surface (Figure 32). In addition, the surrounding silk layers physically hinder rod growth; they tend to extend out only in the horizontal direction when embedded.

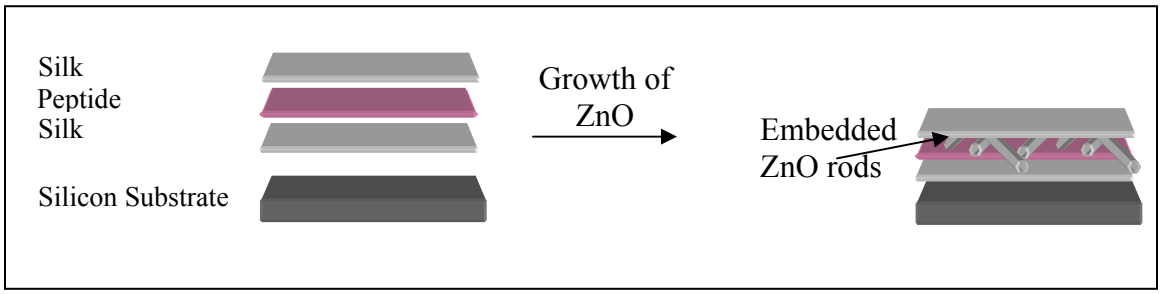

Scheme 4. Film assembly with an embedded peptide layer

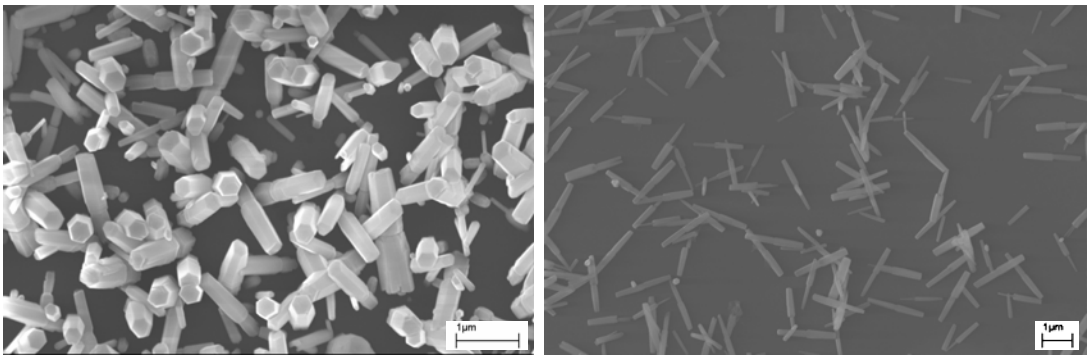

Figure 32. SEM of ZnO grown on (left) $silk_9$+ZnO1 and (right) $silk_9$+ZnO1+$silk_9$ films

An embedded peptide layer was also placed between two drop cast silk films that were each dried in ambient air. Each silk layer was ZnO was grown under the same conditions as above and resulted in nanorods seen in Figure 33. The embedded nanorods are restricted to primarily horizontal directional growth. In addition, the edges do not appear to be the clean facets typical of surface grown nanorods. The diameters were widely varied, typically 200-400 nm.

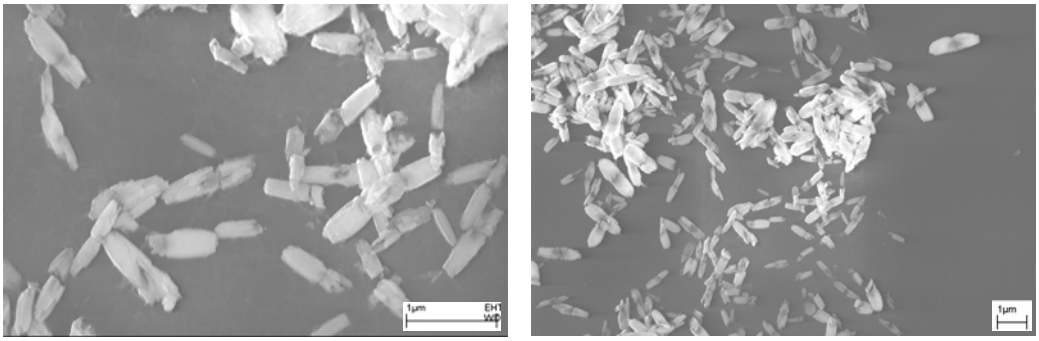

Figure 33. Embedded ZnO grown at a peptide layer between two drop cast silk layers

AFM imaging in Figure 34 shows embedded ZnO grown in a film of silk+ZnO1+silk. The height image (left) shows the ZnO emerging from the surface. However the phase image (right) does not show a significant difference in surface properties of the flat silk surface compared to the rods, indication that a uniform silk layer is covering the zinc oxide. After doing cross sectional analysis, a typical rod had a vertical height of 300-450 nm and a width of 700-920 nm. This is substantially larger than the width that ranged from 100-350 nm seen in SEM. This is due to the layer of silk surrounding each nanorod that increases the rod dimensions in surface morphology

analysis but is generally transparent when analyzed with SEM. Further investigation with XPS was not available for this document but if done in the future, could confirm the surface composition.

The ability to grow embedded zinc oxide here demonstrates that in addition to ZnO1 dictating the placement of growth on a surface, it can also dictate the placement of growth within films. Embedding between thin films with thickness ~50 nm in Figure 32 and thick films at ~500nm in Figure 33 was possible.

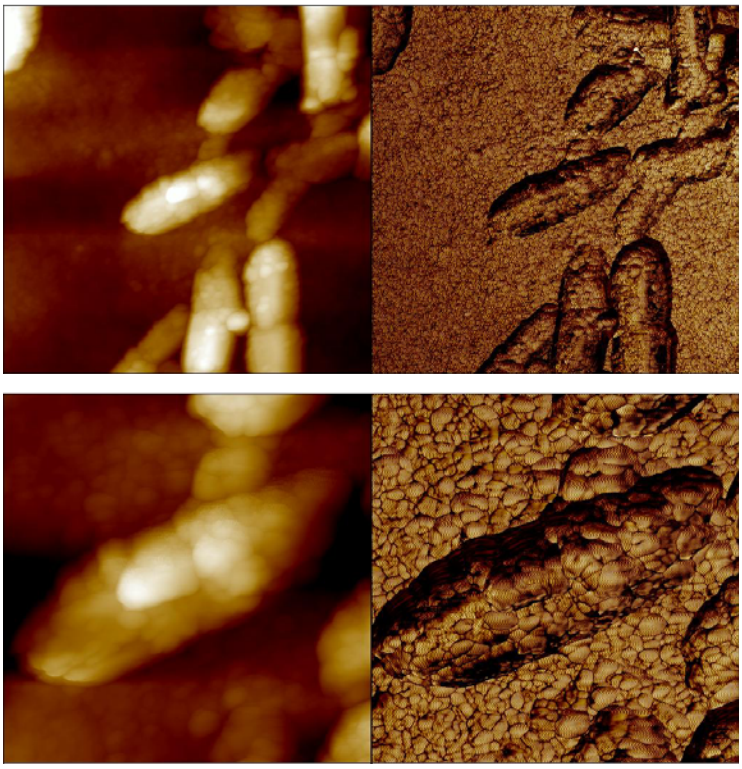

Figure 34. AFM height (left, scale 800nm) and phase (right) images of ZnO grown in a $silk_9$+ZnO1+$silk_9$ film; top is 5µm x 5µm, bottom 2µm x 2µm. Z-scale is 800nm (top) and 550nm (bottom)

Vertical Zinc Oxide Rod Arrays on Polystyrene

So far, we have demonstrated that the selectively binding peptide ZnO1 has the potential for facilitating the growth of zinc oxide nanorods on silk and polymer surfaces, as well as embedded between silk films. Randomly arranged nanorods however are not useful for most applications. Vertical arrays can be applicable. Currently, severe substrate limitations exist because of processing conditions required to achieve vertical nanorod arrays. Vertical nanorods have yet to be grown on completely organic templates. Here we investigate the next step in achieving this goal with a selectively binding peptide: to grow *vertical* nanorods on organic templates. Control of surface density, size, and other parameters will be discussed.

Polystyrene and Peptide Surface

As silk is difficult to process and is stable in water for only a few days, polystyrene was used as a surface for the deposition of ZnO1 peptide and subsequent growth of vertical ZnO rods.

Initial experiments discussed previously used a film spin cast from a solution of silk or polystyrene upon which peptide was drop cast and dried. Silk is very rough as seen in Figure 35. The drop casting method however results in an extremely rough peptide surface and no vertical alignment was ever observed. A smooth template is necessary for vertical nanorod growth dictated by peptide.

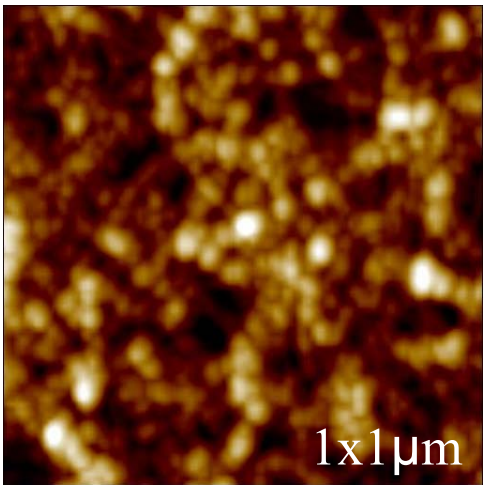

Figure 35. AFM height image of silk film with a roughness of 4.8nm

In an attempt to lower the Roughness Mean Squared (RMS) of the surface, polystyrene was used as an underlying layer and spin casting was employed to deposit peptide. As the quantity of ZnO1 was severely limited and spin casting requires a lot of material, much smaller silicon wafers were used (2.5mm x 2.5mm) such that 5µl of ZnO1 would be sufficient to make a uniform spin cast layer of peptide on each sample.

Figure 36 shows the surface morphology of a PS film spin cast onto a silicon wafer from a 0.2wt % solution. The left is the height image and right is phase. The polystyrene surface RMS was measured to be 0.21 nm. All roughness values were taken over a 1µm x 1µm area. The PS film thickness was measured 6.3 nm with ellipsometry. Contact angle was 79^{o}.

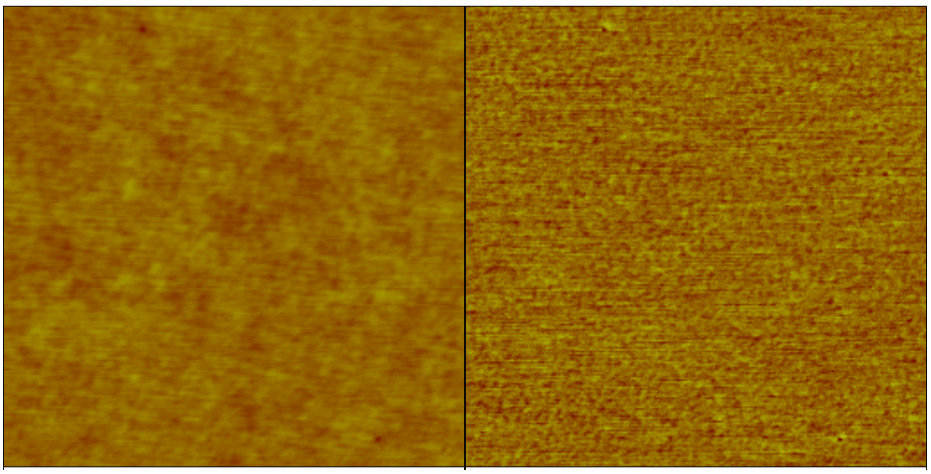

Figure 36. AFM image of polystyrene surface spin cast from 0.2wt% solution (1x1µm scan, z-scale 5nm)

The first attempt to achieve a layer suitable for vertical rod growth, spin casting was used instead of drop casting. The peptide was dropped onto the silicon wafer, left to adsorb to the polymer layer for 15mins, spun dry at 6000rpm, and then rinsed with water. The sample was placed in a small vial of $Zn(NO_3)_2$ and HMT, both at 0.1M concentrations at a 1:1 ratio. The sample was held at room temperature for 24 hours and then the vial was put into an oven at 65^{o}C for 24hrs. The newly formed zinc oxide nanorods were gently rinsed with water and dried under flowing nitrogen air. Using this method, no vertical alignment was observed.

In a second attempt, the peptide was spin cast onto the polystyrene layer but not rinsed. After spinning, the thickness of the peptide layer was measured with ellipsometry to be 3.5 nm, a thick layer for a peptide considering the mass of 1616 Da. Contact angle of the film was reduced to 62^{o}. The resulting surface was smooth with an RMS of 0.26 nm. Figure 37 shows the surface morphology of 20 x 20, 5 x 5, and 1 x 1µm AFM scans. Z scale is 8nm. Interestingly, a circular pattern is formed by the peptide, probably a

result of drying effects. The circular shapes in any case were small in height and were sparse, not significantly increasing the roughness of the overall surface.

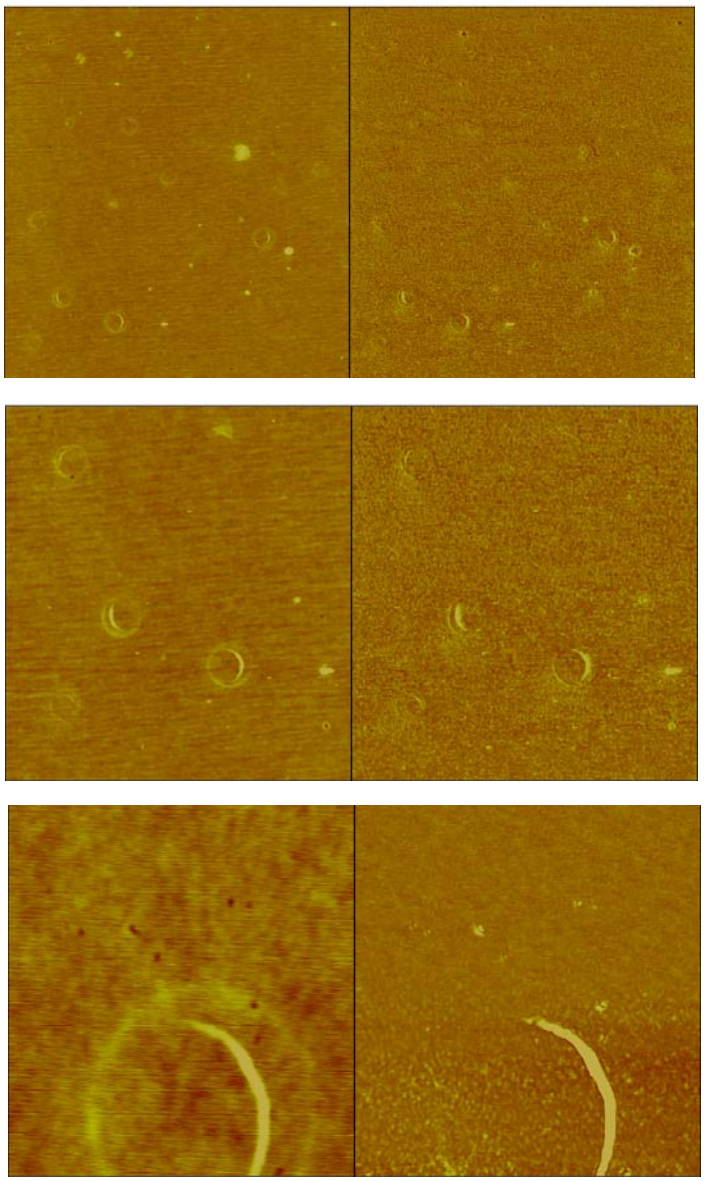

Figure 37. AFM image of ZnO1 spin cast on PS from a A) 20x20 B) 5x5 and C) 1x1µm scan

The sample was put in the vial to grow zinc oxide similarly to the previous attempt but without rinsing the peptide surface before growing zinc oxide. Optical microscopy showed uniform growth across the entire sample surface. Figure 38 SEM images show uniform spatial distribution of vertical ZnO rods with hexagonal cross sections.

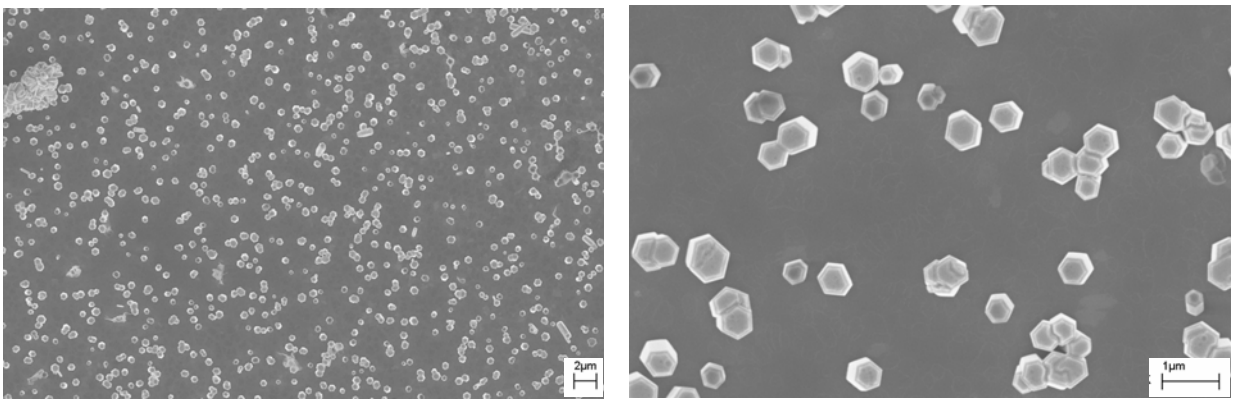

Figure 38. Vertical ZnO rods on PS and an unrinsed peptide layer. Grown in 0.1M zinc nitrate and HMT at RT 24hrs and then 65oC for 24hrs.

In this sample, hexagonal vertical rods were successfully grown at a low temperature of 65˚C with relativel y high density. However, large aggregates fell out of solution as seen in Figure 39. Also, rods were far from monodisperse.

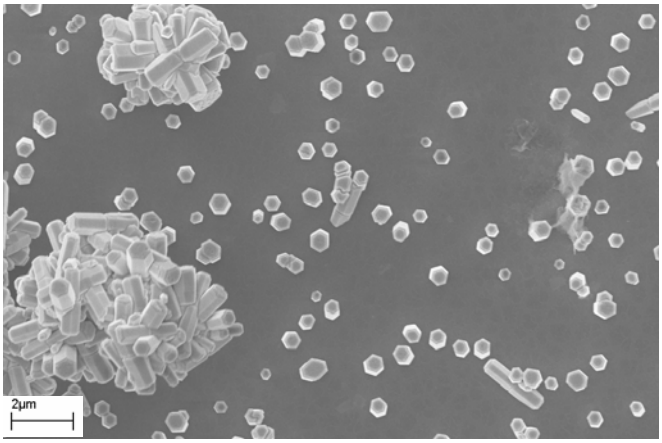

Figure 39. Vertical rods of Figure 38 but showing a different area of large precipitated aggregates which were common on the surface

Controlling Size and Density of Vertical Rods

In previous experiments with ZnO1 on silk, the concentration of zinc nitrate and HMT was decreased and significantly reduced the number of nanorods formed on the surface during a given time. Here, we use growth conditions which hold the time and temperature constant at RT 24hrs, 65^{o}C 24hrs and changed the relative concentrations of zinc nitrate and HMT. Changes to molar concentrations in each trial were done to either zinc nitrate or HMT by using some multiplier on 0.1M while the other component in that trial was held at 0.1M. For these experiments, a small 2.5x2.5mm silicon wafer was used.

Under the selected growth conditions, ZnO precipitates in solution as well as grows from the surface. When the sample is placed at the bottom of a vial, these solution precipitates can settle or adsorb onto the sample. To prevent this, the silicon wafers were placed upside down gently in the zinc nitrate/HMT solution at the air-liquid interface for

all further investigation as illustrated in Scheme 5. In general, results show a decrease in large aggregates as predicted and an increase in monodispersity using this method. Select concentrations and the resulting percent of surface covered with ZnO are summarized in Table 6.

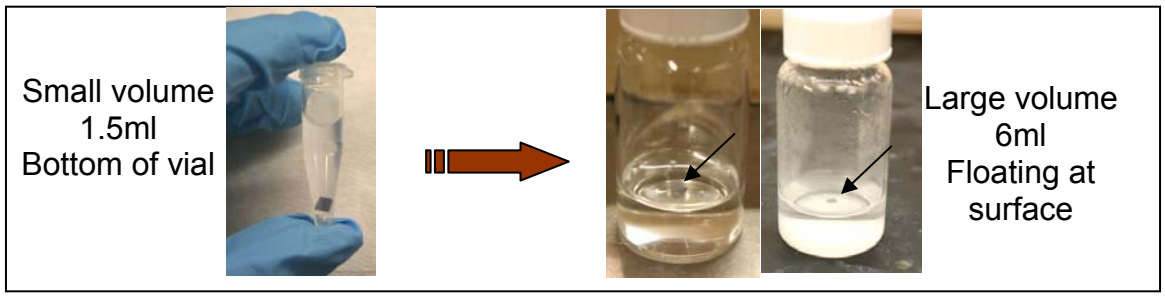

Scheme 5. Setup change in which a larger volume of precursors was used and the placement of the wafer was changed to eliminate large aggregates

Table 6. Matrix to control density of vertical nanorods by changing solution component concentrations

Sample	0.1M Zn(NO3)2	0.1M HMT	% Surface Area Covered	Aspect Ratio
1	x1	x1	**29.9**	**3.25**
2	x1	x4	**12.6**	**-**
3	x1.25	x1	**51.9**	**2.65**
4	x1.5	x1	**73.9**	**2.35**
5	x2	x1	**77.9**	**1.6**

As zinc nitrate was held at 0.1M and HMT concentration was increased, the rod covered area of the surface decreased. By comparing surfaces using HMT at 0.1M and HMT at 0.4M as in Figure 40, rod size is significantly smaller when using a high HMT concentration. Using images with similar magnifications, surface area covered was calculated and compared to the number of rods on each image to get an average rod size for each sample. The diameter of rod when using 0.4M HMT was on average 4.88x smaller than when using 0.1M HMT.

Increasing the concentration of zinc nitrate in Figure 41 increased the surface area covered by rods. Above 0.15M zinc nitrate concentration, the difference in coverage was not significantly increased. At concentrations of 0.1M, 0.125M, and 0.15M however, linear increase in surface density was observed without a change in rod size as illustrated in Figure 42. Interestingly, a linear trend was observed as concentration increased from 1M to 1.5M. In addition, aspect ratios were calculated for each sample. They are summarized in Figure 43. Interestingly, the aspect ratios also saw a generally linear relationship with concentration from 1M to 2M. As concentration increased, the aspect ratios decreased significantly.

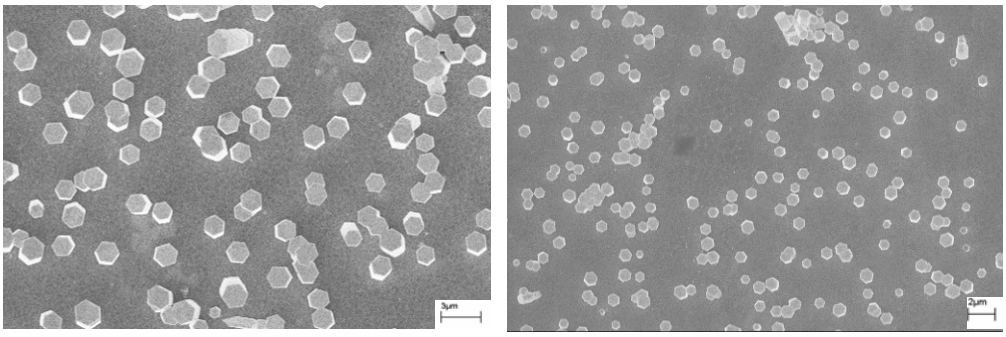

Figure 40. ZnO grown on PS+ZnO1 in (left) 0.1M HMT and (right) 0.4M HMT, combined 1:1 with 0.1M zinc nitrate

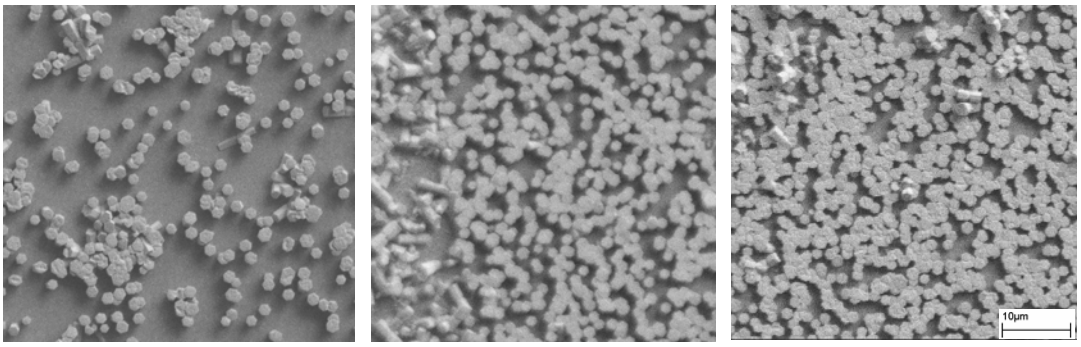

Figure 41. ZnO grown on PS+ZnO1 in 0.1M HMT plus zinc nitrate A) 0.1M B) 0.125M and C) 0.15M

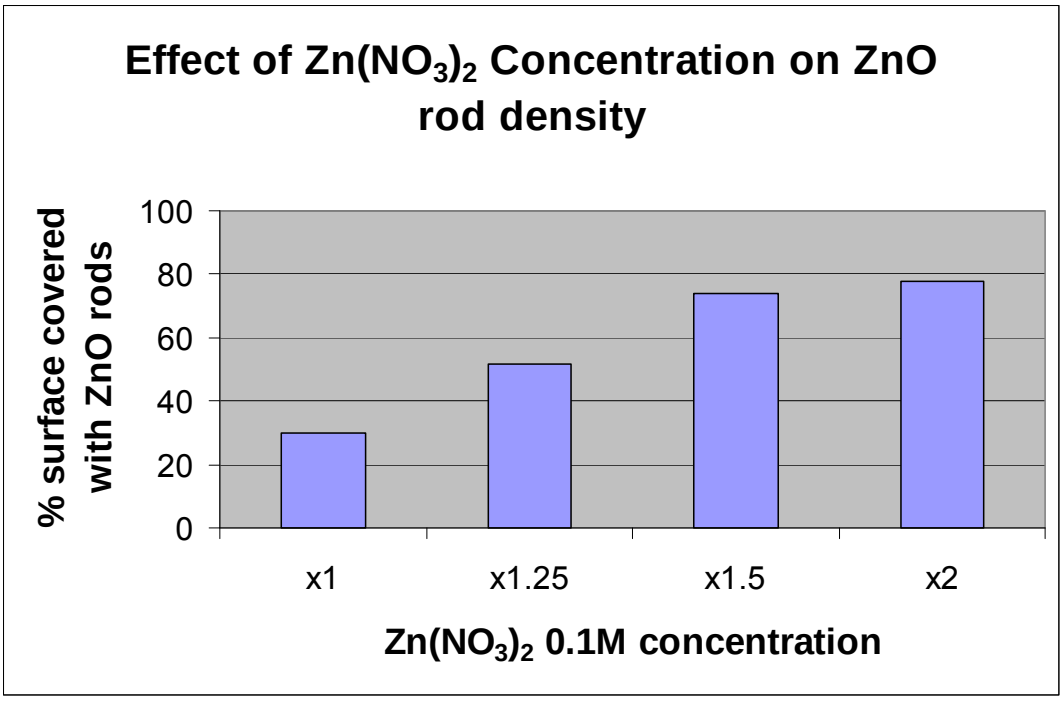

Figure 42. Graph comparing zinc nitrate concentration to percent surface covered by ZnO

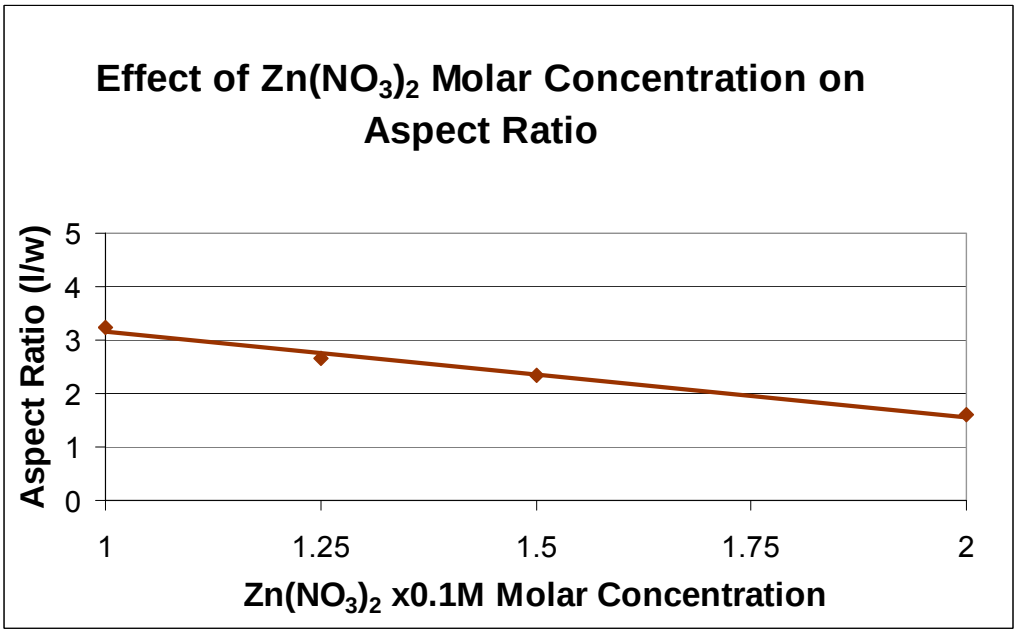

Figure 43. Graph comparing zinc nitrate concentration to aspect ratio

CHAPTER 4

CONCLUSIONS

In this work, we achieved the following:

- Reduction of gold nanoparticles using surface or embedded silk films
- Synthesis of vertical zinc oxide nanorods using polystyrene topped with an organic template of ZnO1 peptide, a zinc oxide selectively binding peptide

Gold nanoparticles were successfully formed from a thin film of silk. More nanoparticles were reduced on a freestanding film than on a substrate-supported film. The two different concentrations and exposure times produced very different reduction effects; a higher concentration and lower time formed uniform 5-10nm spherical particles and the lower concentration with a higher time formed mostly large particles of various shapes. More studies are needed to determine the effect of silk crystallinity, silk film thickness, gold chloride concentration, and exposure time on the size, shape, and density of these nanoparticles. Further investigation would vary the concentration at a specific time or vary the time at a specific concentration to control the density or shape of nanoparticles because prospective applications generally rely on monodisperse, specific shape and size nanoparticles.

A thin film of ZnO1 was successfully created on top of two films, silk and polystyrene. Many parameters were changed to determine the effect on biomineralization

of zinc oxide. These conditions included the deposition method of the peptide film, concentration of both zinc nitrate and HMT in solution, time in solution, temperature of oven, concentration of HMT, concentration of zinc nitrate. Table 7 contains a summary of these results and comparison to literature results of ZnO grown with wet chemical deposition. Note that many of these parameters were not independent, such as temperature/time and size/density.

This system could possibly control achieve vertical nanorods with small widths and high aspect ratios of rods by further tailoring the wet chemical deposition parameters. This would be significant as the density can already be tailored. Interestingly, vertical rods are achieved regardless of the density which contrasts sharply with current methods that require a dense forest of rods to achieve rods where the majority are vertical.

Randomly aligned, primarily horizontal, and primarily vertical ZnO rods were synthesized in this study. To achieve horizontal rods, a film of silk + peptide + silk was used with each film being drop cast. ZnO successfully grew at the location of the peptide film. Due to the physical hindrance from the silk layers, rods were primarily horizontal. Crystal orientation was not determined however and, along with XRD, could give more information about the system with horizontal embedded rods. To achieve vertical rods, a film of polystyrene + peptide was used with each film being spun cast and without rinsing. The smoothness of each later (RMS<1nm) proved extremely important to achieving vertical rods.

Silk and ZnO1 films were shown here to form gold nanoparticles and zinc oxide nanorods at near ambient conditions. The growth of vertical ZnO nanorods on an entirely

organic surface was shown here for the first time. These two successful attempts at biomineralization are encouraging; potential synthesis of other inorganics using protein or designer peptide films could be possible. Peptides and hybrid peptides can be designed for a limitless number of inorganics. We suggest that near ambient condition synthesis of numerous inorganic materials, using peptide templates could be achieved in the near future.

Parameter	Size or Width	Surface Coverage	Aspect Ratio	Literature	Conclusion
ZnO1 presence	Decrease in size	Increase	Same		
Lower HMT & $Zn(NO_3)_2$ concentration	-	Decrease	-	By decreasing both, diameter of rods decrease while the aspect ratio increases [64, 65, 68]	Results were not conclusive. Need to try with conditions favorable for vertical growth.
Higher Temperature	Dependent on time, higher temps need lower times			Similar to literature [73, 74]	
Increase Time in the Oven	Increase in width, size	Increased	Same	Increasing time resulted in a increase in density and length of nanorods [68]	Similar to literature, density was increased and size was increased
Higher HMT only	Decrease in width	-	-	Increasing HMT to zinc nitrate ratio decreases aspect ratio and width [70]	Similar to literature, the width of the rods decreased
Higher $Zn(NO_3)_2$ only	Same width	Linear Increase	Linear Decrease	Increasing zinc nitrate to HMT ratio increases the aspect ratio and width [70]	Contrary to literature, our system decreased the aspect ratio of rods

Table 7. Summary of wet deposition parameters effect on ZnO growth using a film of ZnO1

REFERENCES

1. Vijayakumar, P., Blaker, K., Wieting, R., Wong, B., and Halani, A., *Chemical vapor deposition of zinc oxide films and products*. 1988, Atlantic Richfield Company: United States.

2. Liu, J., Huang, X., Duan, J., Ai, H., and Pinghua, Materials Letters, 2005.

3. Mann, S., *Biomineralization: principles and concepts in bioinorganic materials chemistry*. 2001, New York: Oxford University Press.

4. Sarikaya, M., Tamerler, C., Jen, A., Schulten, K., and Baneyx, F., Nature Materials, 2003. **2**: p. 577.

5. Fowler, C., Shenton, W., Stubbs, G., and Mann, S., Advanced Materials, 2001. **13**(16): p. 1266.

6. Selvakannan, P., Swami, A., Srisathiyanarayanan, D., Shirude, P.S., Pasricha, R., Mandale, A., and Sastry, M., Langmuir, 2004. **20**(18): p. 7821.

7. Sano, K.-I., Yoshii, S., Yamashita, I., and Shiba, K., Nanoletters, 2007. **7**(10): p. 3200.

8. Naik, R., Brott, L., Clarson, S., and Stone, M., Journal of Nanoscience and Nanotechnology, 2002. **2**: p. 1.

9. Naik, R., Stringer, S.J., Agarwal, G., Jones, S., and Stone, M., Nature Materials, 2002. **1**: p. 169.

10. Kroger, N., Dickerson, M., Ahmad, G., Cai, Y., Haluska, M., Sandhage, K., Poulsen, N., and Sheppard, V., Angewandte Chemie, 2006. **45**(43): p. 7239.

11. Aizenberg, J., Advanced Materials, 2004. **16**(15): p. 1295.

12. Slocik, J.M. and Naik, R., Advanced Materials, 2006. **18**: p. 1988.

13. Bloch, A. and Messores, A.S., *Silk Suture*. 1969, Ethicon Inc: United States.

14. Vollrath, F., Madsen, B., and Shao, Z., Proc Biol Sci, 2001. **268**: p. 2339.

15. Shao, Z. and Vollrath, F., Nature, 2002. **418**: p. 741.

16. Perez-Rigueiro, J., Viney, C., Llorce, J., and Elices, M., J Appl Polym Sci, 1998. **70**: p. 2439.

17. Vollrath, F., J Biotechnology, 2000. **74**: p. 67.

18. Heslot, H., Biochimie, 1998. **80**: p. 19.

19. Hakimi, O., Knight, D.P., Vollrath, F., and Vadgama, P., Composites Part B: Engineering, 2007. **38**(3): p. 324.

20. Gosline, J., Guerette, P., Ortlepp, C., and Savage, K., J Exp Biol, 1999. **23**: p. 3295.

21. Sehnal, F. and Zurovec, M., Biomacromolecules, 2004. **5**: p. 666.

22. Kaplan, D., Lombardi, S., Muller, W., and Fossey, S., *Biomaterials*, ed. D. Byrom. 1991: Stockton Press, New York.

23. Cong-Zhao Zhou, F.C.M.J.R.P.Z.-G.L.J.J., Proteins: Structure, Function, and Genetics, 2001. **44**(2): p. 119.

24. Liivak, O., Flores, A., Lewis, R., and Jelinski, L., Macromolecules, 1997. **30**: p. 7127.

25. Guan, Z., Polymer International, 2007. **56**(4): p. 467.

26. Asakura, T., Yao, J., Yamane, T., Umemura, K., and Ulrich, A., Journal of American Chemical Society, 2002. **124**: p. 8794.

27. Canetti, M., Seves, A., Secundo, F., and Vecchio, G., Biopolymers, 1989. **28**: p. 1613.

28. Knight, D.P. and Vollrath, F., Biomacromolecules, 2001. **2**: p. 323.

29. Rotondi, K.S. and Gierasch, L.M., Peptide Science, 2006. **84**(1): p. 13.

30. Termonia, Y., Macromolecules, 1994. **27**: p. 7378.

31. Simmons, A., Michal, C., and Jelinski, L., Science, 1996. **271**: p. 84.

32. Van Beek, J., Hess, S., Vollrath, F., and Meier, B., Proc Natl Acad Sci USA, 2002. **99**: p. 10266.

33. Phillips, D.M., Drummy, L.F., Conrady, D.G., Fox, D.M., Naik, R.R., Stone, M.O., Trulove, P.C., Delong, H.C., and Mantz, R.A., J. Am. Chem. Soc., 2004. **126**(44): p. 14350.

34. Jin, H.-J., Park, J., Karageorgiou, V., Kim, U.-J., Valluzzi, R., Cebe, P., and Kaplan, D.L., Advanced Functional Materials, 2005. **15**: p. 1241.

35. Jiang, C., Wang, X., Gunawidjaja, R., Lin, Y.H., Gupta, M.K., Kaplan, D.L., Naik, R.R., and Tsukruk, V.V., Advanced Functional Materials, 2007. **17**(13): p. 2229.

36. Zarkoob, S., Reneker, D., Eby, R., Hudson, S., Ertly, D., and Adams, W., Polym Preprint, 1998. **39**(2): p. 244.

37. Putthanarat, S., Eby, R., Kataphinan, W., Jones, S., Naik, R.R., Reneker, D., and Farmer, B., Polymer 2006. **47**: p. 5630.

38. He, S., Valluzzi, R., and Gido, S., Int J Biol Macromol, 1999. **24**: p. 187.

39. Hronska, M., Van Beek, J., Williamson, P., Vollrath, F., and Meier, B., Biomacromolecules, 2004. **5**: p. 834.

40. Shao, Z., Hu, X., Frische, F., and Vollrath, F., Polymer, 1999. **40**: p. 4709.

41. Minoura, N., Aiba, S., Higuchi, M., Gotoh, Y., Tsukada, M., and Imai, Y., Biochem Biophys Res Commun, 1995. **208**: p. 511.

42. Sugihara, A., Sugiura, K., Morita, H., Ninagawa, T., Tubouchi, K., and Tobe, R., Proc Soc Exp Biol Med, 2000. **225**: p. 58.

43. Chiarini, A., Petrini, P., Bozzini, S., Pra, I., and Armato, U., Biomaterials, 2003. **24**: p. 789.

44. Min, B., Lee, G., Kim, S., Nam, Y., Lee, T., and Park, W., Biomaterials, 2004. **25**: p. 1289.

45. Gotoh, Y., Tsukada, M., and Minoura, N., J Biomed Mater Res 1998. **39**: p. 351.

46. Chen, J., Altman, G., Karageorgiou, V., Horan, R., Collette, A., and Volloch, V., J Biomed Mater Res A, 2003. **67**: p. 559.

47. Inouye, K., Kurokawa, M., Nishikawa, S., and Tsukada, M., J Biochem Biophys Methods, 1998. **37**: p. 159.

48. Chen, J., Minoura, N., and Tanioko, A., Polymer 1994. **35**: p. 2853.

49. Potiyaraj, P., Kumlangdudsana, P., and Dubas, S., Materials Letters, 2006. **61**: p. 2464.

50. Li, C., Jin, H.-J., Botsaris, G., and Kaplan, D.L., J Mater Res, 2005. **20**(12): p. 3374.

51. Singh, A., Hede, S., and Sastry, M., Small, 2007. **3**(3): p. 466.

52. Dong, Q., Su, H., and Zhang, D., J Phys Chem B, 2005. **109**: p. 17429.

53. Dubas, S., Kumlangdudsana, P., and Potiyaraj, P., Colloids and Surfaces A, 2006. **289**: p. 105.

54. Ikawa, T., Sajiki, H., and Hirota, K., Tetrahedron, 2005. **61**: p. 2217.

55. Zhou, Y., Chen, W., Itoh, H., Naka, K., Ni, Q., Yamaneb, H., and Chuio, Y., Chem Commun, 2001: p. 2518.

56. Jiang, C., Markutsya, S., Pikus, Y., and Tsukruk, V., Nature Materials, 2004. **3**: p. 721.

57. Leong, W., Lee, P., Mhaisalkar, S., Chen, T., and Dodabalapur, A., Applied Physics Letters, 2007. **90**: p. 042906.

58. Feng, X.-X., Chen, J., Yao, J.-M., and Zhang, J.-C., J Appl Polym Sci, 2006. **101**: p. 2162.

59. Feng, X.-X., Zhang, L.-L., Chen, J., Guo, Y.-H., Zhang, H.-P., and Jia, C.-I., Biological Macromolecules, 2007. **40**: p. 105.

60. Panilaitis, B., Altman, G., Chen, J., Jin, H.-J., Karageorgiou, V., and Kaplan, D.L., Biomaterials, 2003. **24**: p. 3079.

61. Kuchibhatla, Progress in Materials Science, 2007. **52**: p. 752.

62. Yang, P., Yan, H., Mao, S., Russo, R., Johnson, J., Saykally, R., Morris, N., Pham, J., He, R., and Choi, H., Journal of Advanced Functional Materials, 2002. **12**: p. 323.

63. Lin, C., Chen, S., and Cheng, S., Journal of Crystal Growth, 2005. **283**: p. 141.

64. Vayssieres, L., Advanced Materials, 2003. **15**: p. 464.

65. Vayssieres, L., Keis, K., Lindquist, S.-E., and Hagfeldt, A., J Phys Chem B, 2001. **105**(3350): p. 3350.

66. Greene, L., Yuhas, B., Law, M., Zitoun, D., and Yang, P., Inorganic Chemistry, 2006. **45**: p. 7535.

67. Andres-Varges, J Chem Soc Faraday Trans, 1990. **86**: p. 959.

68. Ho, G. and Wong, A., Applied Physics A: Materials Science and Processing, 2007. **86**: p. 457.

69. Li, F., Li, Z., and Jin, J., Materials Letters, 2007. **61**: p. 1876.

70. Postels, B., Wehmann, H.-H., Bakin, A., Kreye, M., Fuhrmann, D., Blaesing, J., Hangleiter, A., Krost, A., and Waag, A., Nanotechnology, 2007. **18**: p. 195602.

71. Weintraub, B., Deng, Y., and Wang, Z.L., Journal of Physical Chemistry Letters C, 2007. **111**: p. 10162.

72. Schmidt-Mende, L. and Macmanus-Driscoll, J.L., Materials Today, 2007. **10**(5): p. 40.

73. Ismail, A., El-Midany, A., Abdel-Aal, E., and El-Shall, H., Materials Letters, 2005. **59**: p. 1924.

74. Scrymgeour, D., Sounart, T., Simmons, N., and Hsu, W., Journal of Applied Physics, 2007. **101**: p. 014316.

75. Vayssieres, L., Keis, K., Lindquist, S.-E., and Hagfeldt, A., J Phys Chem B, 2001. **105**: p. 3350.

76. Greene, L., Law, M., Goldberger, J., Kim, F., Johnson, J., Zhang, Y., Saykally, R., and Yang, P., Angew Chem Int Ed, 2006. **42**: p. 3031.

77. Greene, L., Law, M., Tan, D., Montano, M., Goldberger, J., Somorjai, G., and Yang, P., Nanoletters, 2005. **5**: p. 1231.

78. Morin, S., Amos, F., and Jin, S., Journal of American Chemical Society, 2007. **129**: p. 13776.

79. Umetsu, M., Mizuta, M., Tsumoto, K., Ohara, S., Takami, S., Watanabe, H., Kumagai, I., and Adschiri, T., Advanced Materials, 2005. **17**(21): p. 2571.

80. Yamada, H., Nakao, H., Takasu, Y., and Tsubouchi, K., Materials Science and Engineering C, 2001. **14**(1-2): p. 41.

81. Sidorenko, A., Zhai, X., Peleshanko, S., Greco, A., Shevchenko, V., and Tsukruk, V., Langmuir, 2001. **17**: p. 5924.

82. Tsukruk, V. and Bliznvuk, V., Langmuir, 1998. **14**: p. 446.

83. Chiarelli, P. and Al, E., Advanced Materials, 2001. **13**: p. 1167.

84. Cho, J., Char, K., Hong, J.-D., and Lee, K.-B., Advanced Materials, 2001. **13**: p. 1076.

85. Bergman, K. and Gunawidjaja, R., *Schematic of ZnO growth on polymer surfaces experiment*. 2008.

86. Mamedov, A.A. and Kotov, N.A., Langmuir, 2000. **16**: p. 5530.

87. Lemieux, M., Julthongpiput, D., Bergman, K., Cuong, P., Ahn, H.-S., Lin, Y.-H., and Tsukruk, V., Langmuir, 2004. **20**(23): p. 10046.

88. Orendorff, C., Sau, T., and Murphy, C., Small, 2005. **2**(5): p. 636.

89. Kozlowski, L. *Calculation of protein isoelectric point*. 2007 [cited November 26, 2007]; Available from: http://isoelectric.ovh.org/files/practise-isoelectric-point.html#mozTocId496531.

90. Putnam, C. *Protein Calculator v3.3*. 2006 March 28, 2006 [cited February 7, 2008]; Available from: http://www.scripps.edu/cgi-bin/cdputnam/protcalc3.

91. Bowen, R.A. *Protein Hydrophobicity Plots*. [cited January 11th, 2008]; Available from: http://www.vivo.colostate.edu/molkit/hydropathy/index.html.

92. Gupta, M. and Tomczak, M., *Unpublished work: Morphology changes of ZnO using ZnO1 in solution*. 2007.